

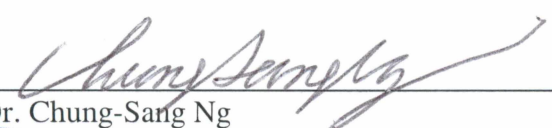
RADIAL AND AZIMUTHAL DYNAMICS OF THE IO PLASMA TORUS

By

Matthew Copper

RECOMMENDED:

  
Dr. Antonius Otto

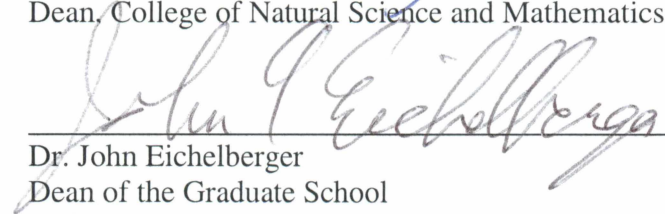
  
Dr. Chung-Sang Ng

  
Dr. Peter Delamere  
Advisory Committee Chair

  
Dr. Curt Szuberla  
Chair, Department of Physics

APPROVED:

  
Dr. Paul Layer  
Dean, College of Natural Science and Mathematics

  
Dr. John Eichelberger  
Dean of the Graduate School

  
Date



RADIAL AND AZIMUTHAL DYNAMICS OF THE IO PLASMA TORUS

A  
THESIS

Presented to the Faculty  
of the University of Alaska Fairbanks

in Partial Fulfillment of the Requirements  
for the Degree of

MASTER OF SCIENCE

By

Matthew Copper, B.A.

Fairbanks, Alaska

May 2015

## Abstract

The moon Io orbits Jupiter emitting neutral particles from its volcanic surface. This emission is ionized and forms the Io plasma torus around Jupiter. The variation of conditions at Io and Jupiter lead to variations in the content of the plasma in the torus. Volcanoes on Io's surface erupt and change the rate of neutral input. Hot electrons (30-100 eV), whose abundances vary in azimuth, create highly ionized species. Radial variation in subcorotation velocities, velocities less than that of the motion of the dipole magnetic field, creates shears while maintaining coherent radial structure in the torus. Poorly understood changes in plasma density circulate through the torus creating the anomalous System IV behavior that has a period slightly longer than the rotation of Jupiter's magnetic field. This thesis summarizes the research that has produced a two-dimensional physical chemistry model, tested several existing theories about subcorotation velocities, System IV variation, and hot electrons, and adopted new methods of Io plasma torus analysis. In an attempt to understand important dynamics, the thesis modeled differing scenarios such as an initialized two-peak structure, a subcorotation profile dictated by mass loading and ionospheric conductivity, and a critical combination of two populations of hot electrons that accurately mimics the observed System IV phenomenon. This model was also used to solve the inverse problem of determining the best fit for the model parameters, neutral source input rate and radial transport rate, using observations of density, temperature, and composition. In addition the thesis shows the need for multi-dimensional modeling and the results from its groundbreaking two-dimensional model.





## Table of Contents

	Page
Signature Page.....	i
Title Page.....	iii
Abstract.....	v
Table of Contents .....	vii
List of Figures.....	ix
List of Tables .....	xi
List of Appendices .....	xiii
Chapter 1 Introduction to the Io Plasma Torus .....	1
1.1 Torus Sources and Sinks.....	2
1.2 Jupiter’s Magnetic Field.....	4
1.3 Reactions in the Io Plasma Torus.....	5
1.4 Hot Electrons.....	7
1.5 Data and Observations .....	8
Chapter 2 One-Dimensional Azimuthal Model.....	13
2.1 One Box Model.....	13
2.2 Azimuthal Model Implementation.....	14
2.3 Validation of the Model.....	16
2.4 Single-Peaked Variation.....	16
2.5 Transient Wave Motion .....	19
2.6 Mass Loading .....	22

2.7	Summary .....	25
Chapter 3	Radial Variation .....	27
3.1	Transport.....	27
3.2	Agreement with Observations.....	29
3.3	Inferences and Analysis .....	30
Chapter 4	Two Dimensional Model.....	34
Chapter 5	Conclusions.....	36
References	.....	39
Appendices	.....	42

## List of Figures

	Page
Figure 1 [Burger, 2003] The configuration of neutral material in the torus. The color bar indicates the density of neutral oxygen.....	2
Figure 2 [Bagenal and Delamere, 2011] The input and output of mass and energy in the torus during Cassini and Voyager. The numbers denote the percentage of total input or output (as shown by the direction of the arrows) that is a result of a given mechanism. Each color represents a different viewing era.....	4
Figure 3 [Schneider and Trauger, 1995] A picture of the torus at different times with Jupiter in the center and Io orbiting. ....	5
Figure 4 [Hess et al., 2011] Output from a model suggestion azimuthal variation of electron mirror ratio and in turn, abundance of hot electrons. The solid line represents the hemispheric average and the other lines represent each hemisphere. ....	6
Figure 5 [Steffl et al., 2008] $S^+$ and $S^{+++}$ mixing ratio variation. Model results are solid lines and observations are colored markers.....	8
Figure 6 [Steffl et al., 2008] Periodograms showing power spectral densities during Cassini observing period. ....	9
Figure 7 [Brown, 1995] Periodograms showing power spectral densities during Voyager observing period. ....	10
Figure 8 [Brown, 1994] The average deviation from corotation and the presence of strong azimuthal shear.....	10
Figure 9 [Steffl et al., 2004] Torus UV emission intensity (in TW on y axis) varied greatly after the Tvashtar eruption. The colors represent UV emissions from different plasma species of the torus and the axis is the day of the year. ..	11

Figure 10	Dual hot electron model output showing azimuthal density variation in particles per cubic centimeter. ....	17
Figure 11	Evolution of two peaked wave structure in the torus. Densities in particles per cubic centimeter. ....	18
Figure 12	The motion of the peaks of $S^+$ and $S^{+++}$ mixing ratios in System III. ....	20
Figure 13	Peak motion in System III with a Gaussian perturbation of hot electron abundance. ....	21
Figure 14	Diagram of the current loop that <i>Pontius and Hill</i> [1982] suggest is responsible for subcorotation in the torus. ....	23
Figure 15	Azimuthal density variations generated by modulating subcorotation velocity with local mass loading. All hot electron variations are stationary in System III. Each frame is ten days apart. ....	24
Figure 16	Azimuthal density variations generated by modulating subcorotation velocity and hot electrons with local mass loading. Each frame is ten days apart. ....	26
Figure 17	The integrated transport time of plasma moving radially in the torus. ..	30
Figure 18	Agreement between output from the model with observation of radial variation. The first five plots are mixing ratios of each species and the last is the radial density profile with observed electron densities. ....	31
Figure 19	Chi squared plots for varied neutral source rate and diffusion coefficient. Thirteen observations were used to calculate chi for each of the seven parameters. ....	33
Figure 20	System IV variations of $S^+$ in two dimensions. In the presence of diffusive radial transport, hot electrons can still produce a single-peaked structure. The time progression of these plots goes left to right. Colors denote local mixing ratio. ....	35

## List of Tables

	Page
1 Table from <i>Steffl et al.</i> [2008]. All timescales are in days. * denotes a fast neutral . . . . .	7
2 Input parameters used to replicate <i>Steffl et al.</i> [2008] results. . . . .	17
3 Input parameters that produce phase shifts in System IV. . . . .	19



## List of Appendices

	Page
Appendix A - One Box Model . . . . .	42
Appendix B - Latitudinal Averaging . . . . .	43



## Chapter 1 Introduction to the Io Plasma Torus

The Io plasma torus is one of the most intriguing places to observe space plasma in our solar system. The torus is constantly fueled by volcanic activity on Io, dissipated through chemistry, and through physical radial and azimuthal transport. The constant source of neutral material makes the torus a partially ionized plasma like one may find in the ionosphere or solar atmosphere. The torus is mainly composed of sulfur and oxygen ions formed from neutral  $\text{SO}_2$  from Io and ionized by electrons. These electrons have varying density in the torus and are kappa distributed in temperature. This kappa distribution is a power law distribution with more electrons in the energetic tail of the distribution. Therefore a fraction of electrons are capable of producing highly ionized states that would not exist otherwise. Though these hot electrons are necessary to produce the highly ionized species present, their source remains a mystery. The combination of all these aspects, makes understanding the Io plasma torus an important part of our understanding of partially ionized space plasmas.

The motion of Jupiter is complex and can have different meanings depending on the context. System I and System II are coordinate systems that are stationary with motion of Jupiter's fluid surface at the equator and high latitudes respectively. For our purposes, Jupiter's surface is irrelevant. Instead we discuss Jupiter using a coordinate system that is stationary in the magnetic dipole field, System III. Plasma that is stationary in this coordinate system are referred to as corotating and plasma that is moving in this coordinate system is subcorotating and moving slower than the magnetic dipole. In addition, there are well known variations of the torus emissions in System III that are completely independent of the other coordinate systems or the interactions between coordinate systems [Dessler, 1983]. The coordinate system in which these variations are stationary is known as System IV. We will rely on System III and System IV to describe torus dynamics.

There are many unanswered questions regarding the Io plasma torus that we intend to investigate. What factors contribute most to azimuthal variation of observed UV emissions?

What could cause variation of observed torus behavior over time? Is mass loading responsible for observed deviation from corotation, rotation with the magnetic dipole, in the plasma? What is responsible for variations in System IV [Brown, 1995; Steffl et al., 2008]? We use our two-dimensional model of the torus to learn more about the torus and how it behaves in radius, azimuth, and time. By answering these questions we can advance our understanding of the Io plasma torus, Jupiter, and partially ionized plasma dynamics in large magnetospheres.

### 1.1 Torus Sources and Sinks

Io is the most volcanically active body in our solar system [Bagenal et al., 2004; Schneider and Bagenal, 2007]. It ejects approximately one tonne of mass every second from the surface and its volcanoes, which can escape Io to become a source of neutral material for the torus. These volcanic eruptions predominantly eject  $\text{SO}_2$ . Io circles Jupiter once every 42.5 hrs while the time it takes to ionize the neutral material is much longer. The neutral material moves at Keplerian velocity close to Io's orbit and produces neutral clouds as shown in Figure 1. These neutral clouds move with Io at 57 km/s in System III, the magnetic coordinate system. The period of Io's orbit is short enough compared to chemical timescales that the location of Io has only negligible affect on the local torus composition.

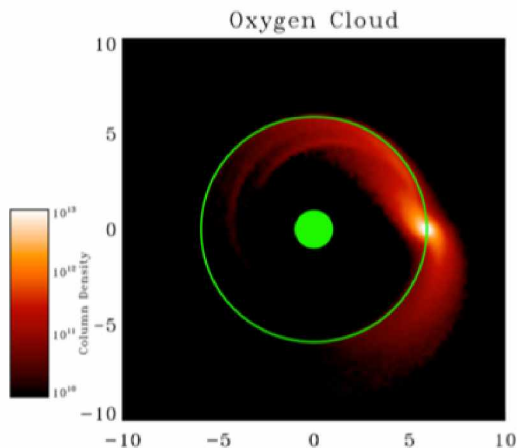


Figure 1: [Burger, 2003] The configuration of neutral material in the torus. The color bar indicates the density of neutral oxygen.

When neutral material is ionized, it becomes confined in the magnetic field and must satisfy the frozen-in condition if ideal magnetohydrodynamic (MHD) approximations are valid. These newly formed ions are known as pickup ions. Jupiter and its magnetic field makes one rotation every 10 hr, much faster than the 42 hr orbit of Io. This means that neutral material must be accelerated from 17 km/s, or Keplerian velocity, to approximately 74 km/s, the magnetic frame of reference. The process of momentum transfer from Jupiter to the pickup ions is known as mass loading. Fast neutrals, or energetic neutrals, are created when accelerated ions collide with neutral particles and produce a neutral particle through charge exchange. The neutral particle will move at the same speed as the ion was previously, but will not be confined by the magnetic field. This neutral atom will have escape velocity and this reaction will act as loss mechanism for neutral material.

In addition to moving around Jupiter with the magnetic field, ions are transported outward, creating a plasma disk. The plasma is subjected to shear flows and changing conditions as it is transported radially and eventually exits the magnetosphere. This is a dominant, but poorly understood, loss mechanism of the torus. Because charge exchange produces an ion for every ion consumed, it is not a loss or source mechanism for ion mass.

Figure 2 details some other loss mechanisms for mass and energy during Voyager and Cassini observations. Notice the change in how mass and energy are input and output from the torus at different times. Also notice the energy content associated with the hot electrons that make up a small fraction of the total electron population. The ion population also causes heating of the thermal electrons through Coulomb collisions. The rest of the energy input is from momentum transfer when new ions are made from neutral material. Most energy is lost through UV emissions, which can account for energy loss at a rate of 1-2 terawatts, while the rest is lost as material exits the system taking thermal energy with it.

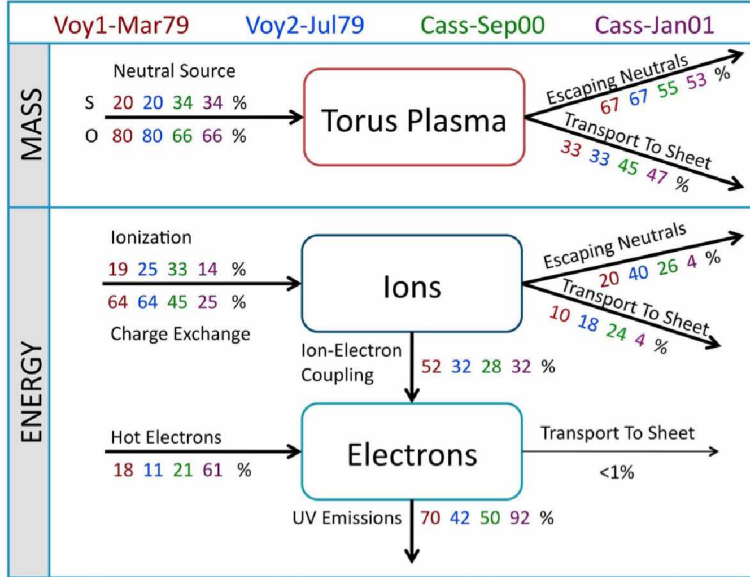


Figure 2: [Bagenal and Delamere, 2011] The input and output of mass and energy in the torus during Cassini and Voyager. The numbers denote the percentage of total input or output (as shown by the direction of the arrows) that is a result of a given mechanism. Each color represents a different viewing era.

## 1.2 Jupiter's Magnetic Field

The magnetic field of Jupiter is not perfectly dipolar and is offset and tilted from the axis of rotation [Hess *et al.*, 2011; Connerney *et al.*, 1998; Connerney, 2007]. The tilt causes the plasma torus to have an apparent wobble when viewed from a distance, as shown in Figure 3. The torus plasma is centrifugally confined to a point on the magnetic field that is farthest from the spin axis, creating a torus that is tilted with respect to the neutral cloud and intersects at  $110^\circ$  and  $280^\circ$  in System III. System III is a coordinate system that is based on the magnetic field orientation of Jupiter rather than the fluid topology. The separation between neutrals and plasma can, in principle, affect the chemistry and, as a result, torus composition.

The higher order magnetic moments of the Jovian magnetic field also result in characteristics that vary in azimuth as shown in Figure 4. Specifically, electron mirror ratios depend on the magnetic field strength near Jupiter and directly affect the rate of hot electron loss by precipitation. For more information see the Section 1.4. The VIPAL model, used in

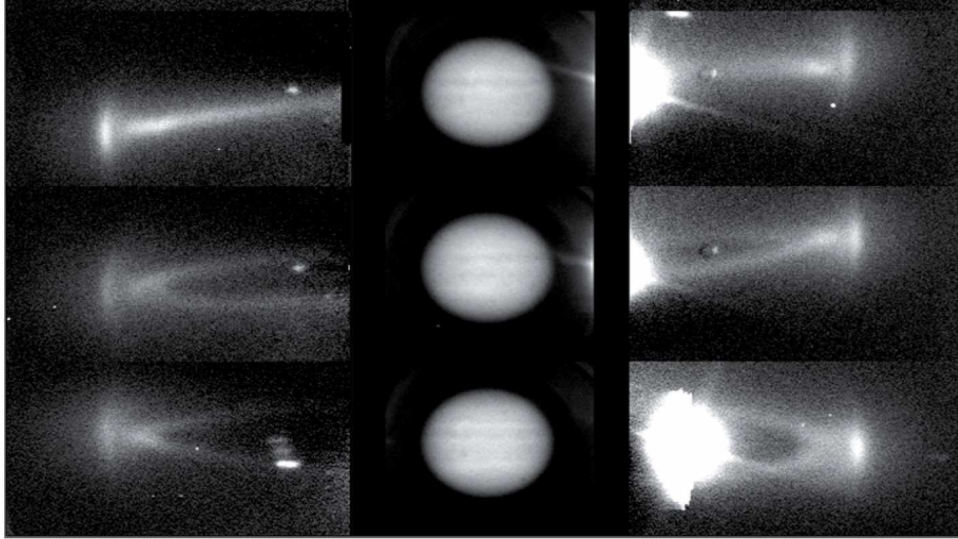


Figure 3: [Schneider and Trauger, 1995] A picture of the torus at different times with Jupiter in the center and Io orbiting.

Hess *et al.* [2011], was constrained by the intensity of Io’s auroral footprint which can be used to infer the loss cone and, in turn, mirror ratio. Since many reactions depend on the electron population, these changes in magnetic field strength can have a clear impact on torus composition.

### 1.3 Reactions in the Io Plasma Torus

The chemical timescales in the inner torus make it the dominating driver of fluctuations. Seventeen different reactions transform the torus. The reaction rates are functions of temperatures and densities of the constituents. Nominal timescales for torus reactions and other mechanisms are shown in Table 1. Creation of pickup ions adds energy to the torus through the magnetic field and coupling with Jupiter’s rotation. Reactions constantly mutate species from one to another and allow for the creation and loss of the different ion species.

The presence of highly ionized species, such as  $S^{+++}$  and  $O^{++}$ , indicates that there must be hot electrons present with temperatures that are higher than the ionization potentials ( $\sim 30\text{eV}$  for  $S^{++}$ ). The electrons have a kappa distribution with a small fraction being hot electrons and the rest being thermal electrons which are on average  $\sim 5\text{ eV}$ , warm enough

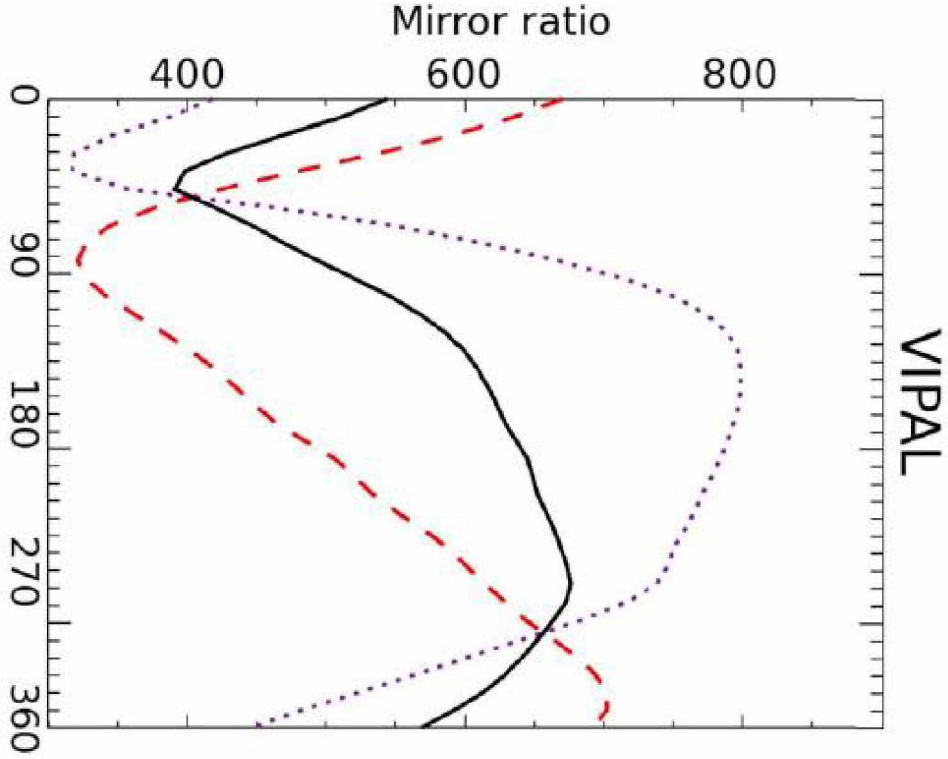


Figure 4: [Hess *et al.*, 2011] Output from a model suggestion azimuthal variation of electron mirror ratio and in turn, abundance of hot electrons. The solid line represents the hemispheric average and the other lines represent each hemisphere.

to maintain a plasma dominated torus. The thermal electron temperature is maintained through Coulomb coupling with ions and hot electrons [Shemansky, 1988]. The coupling of hot electrons to thermal electrons has a timescale of tens of minutes. For our purposes we approximate the kappa distributed electrons as a Maxwellian thermal population at 5 eV and a Maxwellian hot electron population at 30-70 eV, which accounts for only a very small fraction of the total electrons. By using two Maxwellian distributions we can simplify the calculations and allow for the generation of highly ionized plasma involving hot electrons (see Huba [2013] for thermal Coulomb coupling calculations of Maxwellian populations). The abundance of hot electrons varies throughout the torus even with a thermal electron density that is mostly uniform in azimuth [Steffl *et al.*, 2008].



Table 1: Table from *Steffl et al.* [2008]. All timescales are in days. \* denotes a fast neutral

Loss mechanism	S(I)	S(II)	S(III)	S(IV)	O(I)	O(II)	O(III)
Thermal $e^-$ impact ionization	0.8	16.0	463	10400	6.4	926	70700
Hot $e^-$ impact ionization	15.9	43.0	128	338	43.5	168	438
Recombination	–	1410	324	123	–	4050	1330
$S^+ + S^{2+} \rightarrow S^{2+} + S^+$	–	3.0	10.4	–	–	–	–
$S + S^+ \rightarrow S^+ + S^*$	5.0	85.2	–	–	–	–	–
$S + S^{2+} \rightarrow S^+ + S^+$	105	–	6240	–	–	–	–
$S + S^{2+} \rightarrow S^{2+} + S^*$	4.0	–	240	–	–	–	–
$S + S^{3+} \rightarrow S^+ + S^{2+}$	14.0	–	–	142	–	–	–
$O + O^+ \rightarrow O^+ + O^*$	–	–	–	–	2.6	43.3	–
$O + O^{2+} \rightarrow O^+ + O^+$	–	–	–	–	627	–	1070
$O + O^{2+} \rightarrow O^{2+} + O^*$	–	–	–	–	60.4	–	104
$O + S^+ \rightarrow O^+ + S^*$	–	8510	–	–	1990	–	–
$S + O^+ \rightarrow S^+ + O^*$	10.8	–	–	–	–	734	–
$S + O^{2+} \rightarrow S^+ + O^+$	13.9	–	–	–	–	–	95.7
$S + O^{2+} \rightarrow S^{2+} + O^+ + e^-$	20.1	–	–	–	–	–	138
$O + S^{2+} \rightarrow O^+ + S^+$	–	–	205	–	13.8	–	–
$O^{2+} + S^+ \rightarrow O^+ + S^{2+}$	–	262	–	–	–	–	105
$O + S^{3+} \rightarrow O^+ + S^{2+}$	–	–	–	24.4	9.6	–	–
$O^{2+} + S^{2+} \rightarrow O^+ + S^{3+}$	–	–	376	–	–	–	43.4
$S^{3+} + S^+ \rightarrow S^{2+} + S^{2+}$	–	585	–	346	–	–	–
Radial transport	–	62.0	62.0	62.0	–	62.0	62.0
Total of all loss processes	0.5	2.2	7.3	12.8	1.3	20.9	12.5

#### 1.4 Hot Electrons

As a result of the variation of the magnetic field, hemispherically averaged mirror ratios change in System III. The mirror ratio affects the hot electron population because hot electrons can have the energy to precipitate, assuming a pitch angle scattering mechanism. When the magnetic field is stronger, more hot electrons can remain in the torus and the density of hot electrons increases. Since hot electrons move in System III, one would expect a larger fraction of hot electrons to enter the loss cone when they reach a System III longitude that has a weaker magnetic field. The hot electron content should remain uniform throughout System III unless hot electrons were readily generated. This must be the case as observed variations in plasma abundance in System III can only be explained by varying hot electron fraction.

In addition to System III, hot electrons are varied in System IV [*Steffl et al.*, 2008]. System IV is the quasi-periodicity that has a slightly longer period than System III. While System III and its variations are well understood, System IV is merely observed without an agreed upon explanation. The variation in composition and intensity from the torus is the

observable signature of System IV. However, those variations have a frequency that changes and has been known to phase shift [Brown, 1995]. Either through changes in rates of hot electron creation or loss, it is believed that System IV affects the abundance of hot electrons. This results in a population of hot electrons that travels in System III at  $\sim 1$  km/s.

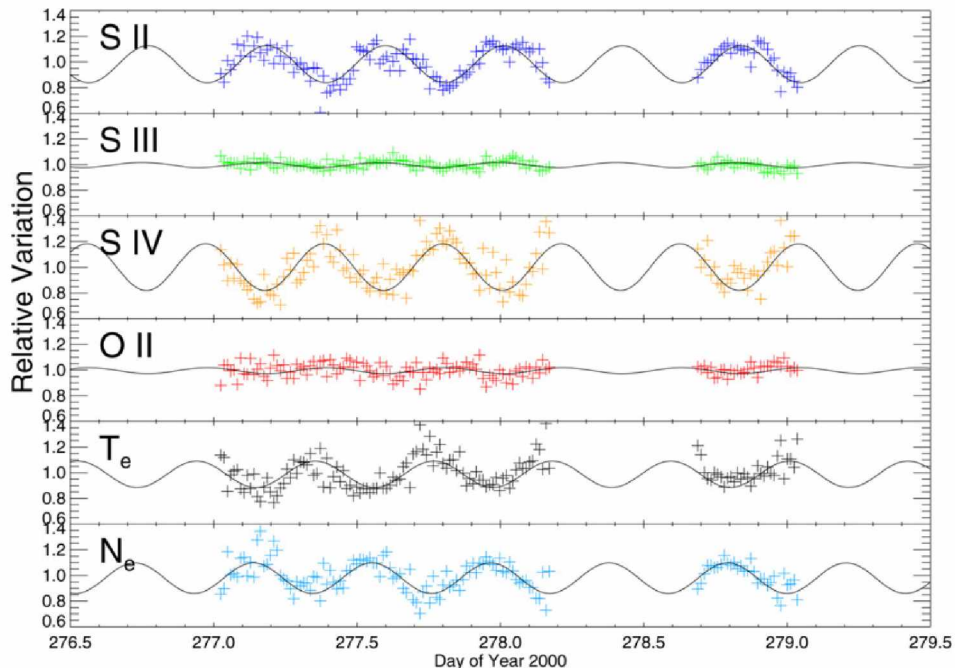


Figure 5: [Steffl *et al.*, 2008]  $S^+$  and  $S^{+++}$  mixing ratio variation. Model results are solid lines and observations are colored markers.

Figure 5, from Steffl *et al.* [2008], shows that mixing ratio variations of  $S^+$  and  $S^{+++}$  are always  $180^\circ$  out of phase. This supports the conclusion that hot electrons are responsible for the peaks in mixing ratios, because areas of increased  $S^{+++}$  are generated through reactions that consume  $S^+$ . Any non-chemical explanation would likely create peaks that are in phase.

### 1.5 Data and Observations

The torus has a very sporadic observation set. In situ data have come from Voyager, Galileo, and Cassini. Observations have also been made from Earth and the Hubble Space Telescope. The EXCEED spectrometer on board the Hisaki satellite mission is going to be one of the longest continuous data sets that include imaging of the Io plasma from outside



Earth's atmosphere [Yoshioka *et al.*, 2014]. Data from EXCEED are still not widely public information, but we hope that it will shed light on long term trends in the torus. The data most useful for our purposes are EUV imaging from outside Earth's atmosphere because they show large scale trends over longer intervals than other data sets. In particular we use the Voyager and Cassini data sets.

System IV variation is easily detected through imaging of the torus. The variation in plasma density results in an observable variation in emissions. The wavelength of these emissions can be associated with a particular ion species and densities of all the species can be inferred through UV observations of the torus. Figure 6 and 7 show the existence and frequency of System IV in the torus.

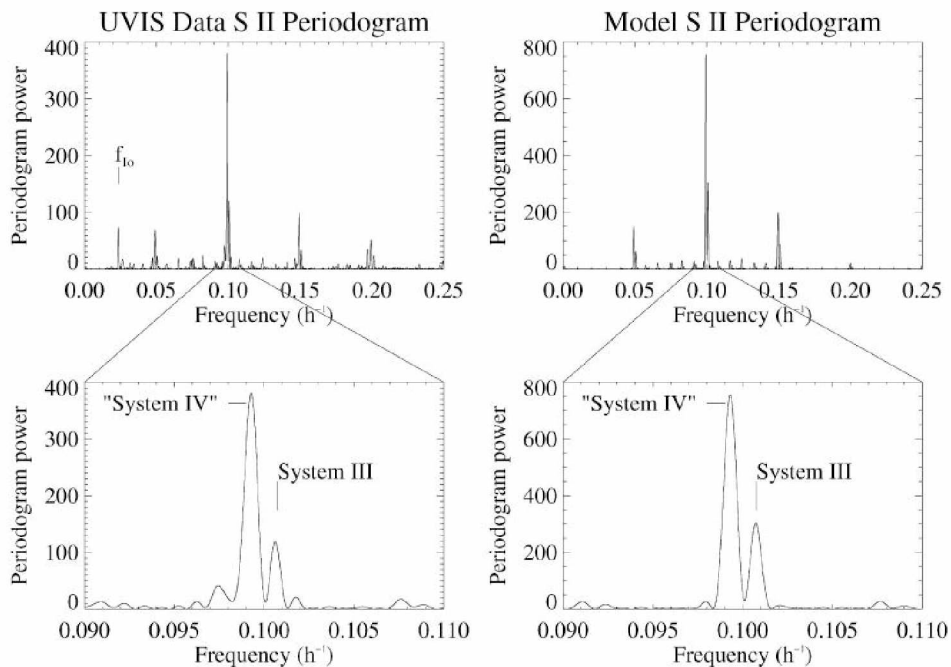


Figure 6: [Steffl *et al.*, 2008] Periodograms showing power spectral densities during Cassini observing period.

Between the Voyager and Cassini observations System IV changed frequency. The System IV period has been observed at 10.224 hr by Sandel and Dessler [1988], 10.214 hr by Brown [1995], and 10.07 hr by Steffl *et al.* [2008]. Since System IV periodicity changes in time, we should expect some variation in our model as well. The timescale of this change may be

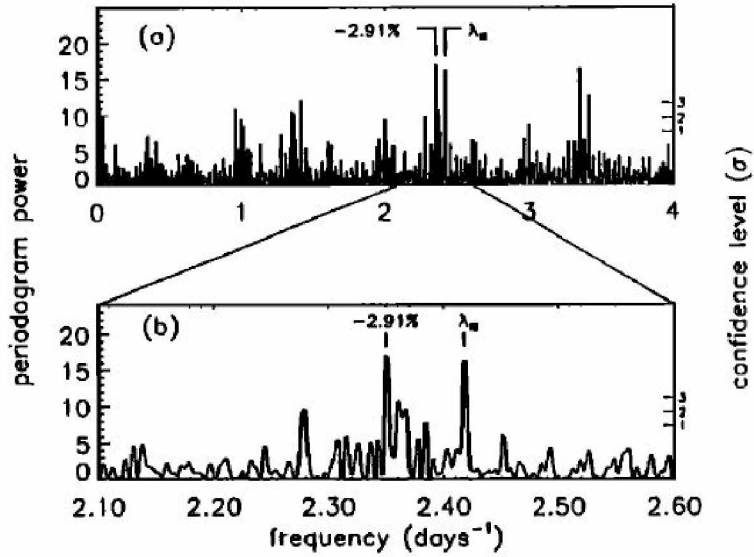


Figure 7: [Brown, 1995] Periodograms showing power spectral densities during Voyager observing period.

months or years, and may be an observable behavior in our model as well.

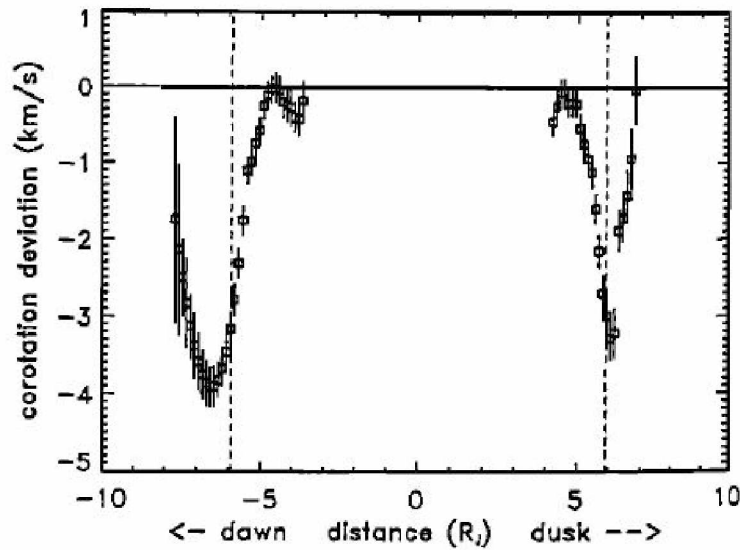


Figure 8: [Brown, 1994] The average deviation from corotation and the presence of strong azimuthal shear.

Observations also show that azimuthal flows in the torus are subcorotational and that the subcorotation velocity changes as a function of radius. Figure 8 shows the subcorotation as a function of radial distance on dusk and dawn sectors. With azimuthal flows that vary

radially, one would expect that variations from the inner torus would “stir” and the outer torus would be more uniform. However, this is not the case and azimuthal variations remain coherent beyond  $7.5 R_J$  [Brown, 1995],  $\sim 1.5 R_J$  beyond the inner boundary of the torus. This means that azimuthal variation beyond the inner torus is not just a result of transport from high density regions. The structure must persist as a result of an active mechanism for modifying plasma properties at radial distances greater than  $6.5 R_J$ .

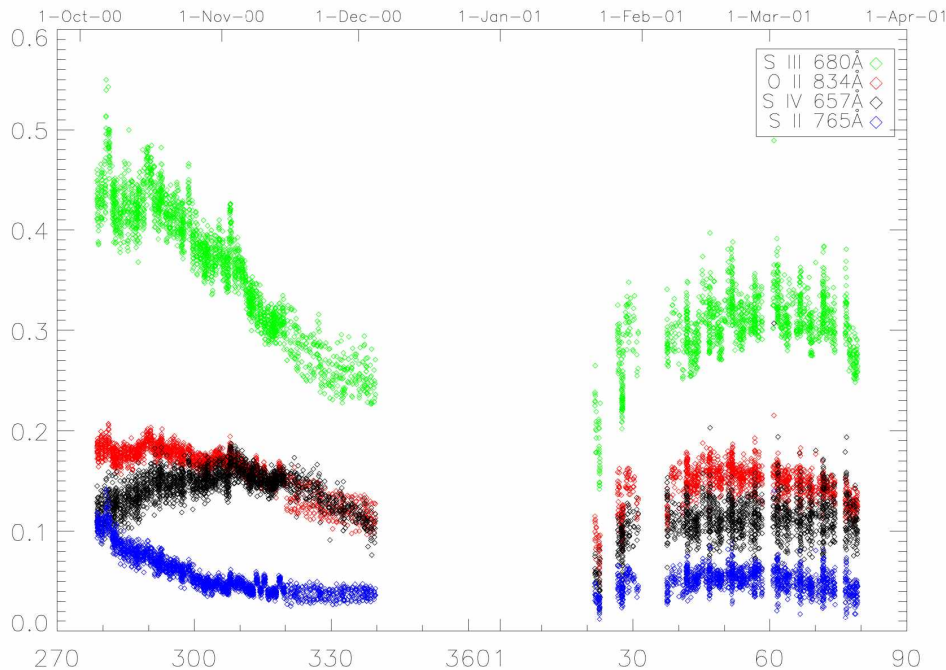


Figure 9: [Steffl *et al.*, 2004] Torus UV emission intensity (in TW on y axis) varied greatly after the Tvashtar eruption. The colors represent UV emissions from different plasma species of the torus and the axis is the day of the year.

Variations in the torus as a result of volcanic activity on Io have also been observed. Observations during the Cassini viewing period show a dissipation of torus emissions following the Tvashtar eruption [Steffl *et al.*, 2004], as shown in Figure 9. Observations only show the end of the eruption and emissions changing by a factor of two over two months. Figure 9 shows these changes and separates by wavelength for each species. Anomalous or abnormal behaviors previously observed may be explained by large rapid variation of the volcanoes on Io and in turn, the neutral source to the torus.

Our research intends to take this information and model the physical chemistry of the Io plasma torus constrained by observations. With such a model we can test hypotheses and determine their validity. In this way we can learn the most from what observations we have of the torus and be better prepared to use and analyze future observations. While other models have looked at the torus in azimuth or radius, we will create a two-dimensional model so that the dynamics of each dimension work simultaneously as they would in the torus. We believe that a two-dimensional model is essential to accurately modeling the torus because of the coupling of effects found in azimuth and radius. One example of this coupling would be azimuthal variations being damped by diffusive radial transport which will act more readily in enhanced density regions of the inner torus. In addition, some unanswered questions are two-dimensional in nature. We hope to be able to address the long-standing System IV quasi-periodicity of the Io plasma torus.

## Chapter 2 One-Dimensional Azimuthal Model

The first step in the research is to create a one-dimensional model to investigate the fluctuations of the torus in azimuth. The foundation of this one-dimensional model was a one box model [Delamere and Bagenal, 2003]. The one box model would account for input and output and model overall composition of the torus with no regard for spatial variation. With a one box model completed and validated, the one box model will be duplicated and modified to simulate individual slices of the torus. With each slice simulating chemical compositions over time, they will communicate between each other to create azimuthal transport. For our particular situation, this will allow us to introduce parallelism to the model and allow each “box” to run on its own processor. With the model completed and validated, we will investigate changes in composition, the single-peaked structure, and the possible affect of mass loading in the torus.

### 2.1 One Box Model

The one box model that is used as the foundation for the research was originally created by Delamere and Bagenal [2003] and our model will be an adaptation of a more recent latitudinally averaged one box model made by Steffl *et al.* [2008], see Appendix B for more information on latitudinal averaging. The model prescribes a volumetric neutral source (in  $cm^{-3}s^{-1}$ ) and radial transport rates and uses a lookup table for radiative rate coefficients and published reaction rates to model chemical change in the inner torus. Hot electrons are described using a hot population and a thermal population. The changes in chemical composition are calculated using the second order Improved Euler method.

Chemical reaction rates are based on the abundance and temperature of the reactants. Seventeen different reactions are accounted for in this model their nominal timescales are listed in Table 1. Radiative rate coefficients and reaction rates are provided in the CHIANTI database [Landi *et al.*, 2013]. To model chemistry changes in the torus we simply consider

the sources and losses of each species. Radial transport is counted as a simple loss timescale at this point. Chemical reaction rates are used as loss rates for consumed species and source rates for species yielded. Neutral species are only consumed by reactions because reactions that generate neutrals only generate fast neutrals with an assumed escape velocity. However, neutrals have a source in the form of the neutral source rate from Io.

To iterate densities through time we use the Improved Euler method as shown in Equations 1 through 3.

$$\frac{\partial n}{\partial t} = f(t, n) \quad (1)$$

$$n^{j+1} = n^j + \frac{\Delta t}{2} [f(t^j, n^j) + f(t^j + \Delta t/2, n^j + \frac{\Delta t}{2} f(t^j, n^j))] \quad (2)$$

$$n^{j+1} = n^j + \frac{\Delta t}{2} (f^j + f^{j+1/2}) \quad (3)$$

In the previous equations,  $n$  is the density of the species,  $f(t^j, n^j)$  is the overall source or loss of a given species, and the superscript denotes the time step. We essentially calculate the amount of a species as a precursor and use the precursor to calculate an improved estimate and average the result of both. The time step can be adjusted in the code but is on the order of 1000 seconds, much shorter than chemical and physical timescales which are several hours to days as shown in Table 1. For more information on the equations governing the one box model, see Appendix A.

## 2.2 Azimuthal Model Implementation

With the one box model completed and validated, it is easy to create a one-dimensional model in parallel. To do this, we run the one box model on different nodes adjusting longitude, volume, and neutral source for the new situation. The longitude for each node, which we will refer to as bins moving forward, is set based on the node id. Each bin's volume is uniform and is simply the volume of the entire torus divided by the number of bins and likewise for neutral source rate. The source is treated as ubiquitous because the local variation is negligible due to long chemical and physical timescales that are on the

order of ten days.

The bins are locked in System III and the subcorotating plasma must advect from one bin to another as it moves in System III. To do this we use communication between bins to implement the upwind scheme as shown in Equation 5,

$$\frac{\partial n}{\partial t} = -\frac{\partial(un)}{\partial x} = -u\frac{\partial n}{\partial x} \quad (4)$$

$$n_i^{j+1} = n_i^j + \frac{u\Delta t}{\Delta x}[n_{i-1}^j - n_i^j] \quad (5)$$

where  $u$  is the flow velocity,  $n$  is the density,  $\Delta x$  is the arc length of the azimuthal bin, and subscripts denote spatial index. This discretization assumes a constant flow velocity. The upwind scheme works efficiently and takes advantage of the subcorotating nature of the Io plasma torus. The upwind scheme is first order accurate and stable when the Courant-Friedrich-Lewy condition (CFL) is met, such that  $\frac{u\Delta t}{\Delta x} < 1$ . This method is consistent with the linear convection equation with an additional numerical diffusion term that we neglect because gradients in azimuths are expected to be small. Each processor receives density values from the processor upwind of itself and sends density values to the processor downwind such that each processor uniquely sends and receives the same amount of information. If a piece of data is sent and not received, the model would hang and fail to complete. The upwind scheme as shown in Equation 5 is for a uniform flow speed, but since densities vary throughout the torus the amount of plasma transported can vary for each azimuthal bin. The flow rate  $u$  is the prescribed subcorotational velocity of the plasma because the model is in the System III, or rigidly corotating, frame of reference. The subscript,  $i$ , denotes a spatial cell and also corresponds to a processor. Because we are dealing with azimuth, the processors are circularly arranged and the processor to the left of processor 0 is  $N - 1$  and the processor to the right of  $N - 1$  is 0, where  $N$  is the number of processors. The superscript,  $j$ , denotes the time step. This notation will be used to describe numerical methods throughout this document.

Results taken from our one-dimensional model were compared with the previous one-dimensional model results [Steffl *et al.*, 2008]. It is clear to us that the model produces similar results and that it is in agreement with observations. In addition, inputs were nearly the same.

### 2.3 Validation of the Model

A previous azimuthal model was created by Steffl *et al.* [2008] that used two hot electron populations to model System IV dynamics. One population was stationary in System III and the other was stationary in System IV and moving in System III with a prescribed angular velocity. The equation we use for hot electron variation in System III is,

$$f_h(t, \lambda_{III}) = f_{h_0}[1 + A_{\lambda_{III}} \cos(\lambda_{III} - \phi_{\lambda_{III}}) + A_{\lambda_{IV}} \cos(\lambda_{III} - \phi_{\lambda_{IV}} - \omega t)] \quad (6)$$

where  $f_h$  is the hot electron fraction at a given time and longitude,  $f_{h_0}$  is the prescribed average hot electrons fraction,  $A$  is the amplitude of the variation,  $\phi$  is the longitude of the peak, and  $\omega$  is the angular velocity of System IV in System III, with subscripts that denote the coordinate system. The addition of hot electron variation in System IV is an ad-hoc explanation of System IV variation that is not motivated by a proposed mechanism for increased hot electron abundance. We will validate our output by comparing with the Steffl *et al.* [2008] results. The goal is to recreate the System IV trends achieved. To do this we employ the same hot electron model with parameters as stated in Table 2 and uniform initial plasma densities. Our results are shown in Figure 10. The period, and phase difference between  $S^+$  and  $S^{+++}$  are both similar to reported values from Steffl *et al.* [2008].

### 2.4 Single-Peaked Variation

With the model working as expected, we tested hypotheses and investigated the behavior of the model, comparing to observations and testing theories of spatial variation. It is well



Table 2: Input parameters used to replicate *Steffl et al.* [2008] results.

Parameters	Values
Neutral Source Rate	$2 \times 10^{28} s^{-1}$
Hot Electron Fraction ( $f_{h_0}$ )	0.3%
System III Hot Electron Variation ( $A_{\lambda_{III}}$ )	40%
System IV Hot Electron Variation ( $A_{\lambda_{IV}}$ )	30%
Subcorotation Velocity	1.0km/s

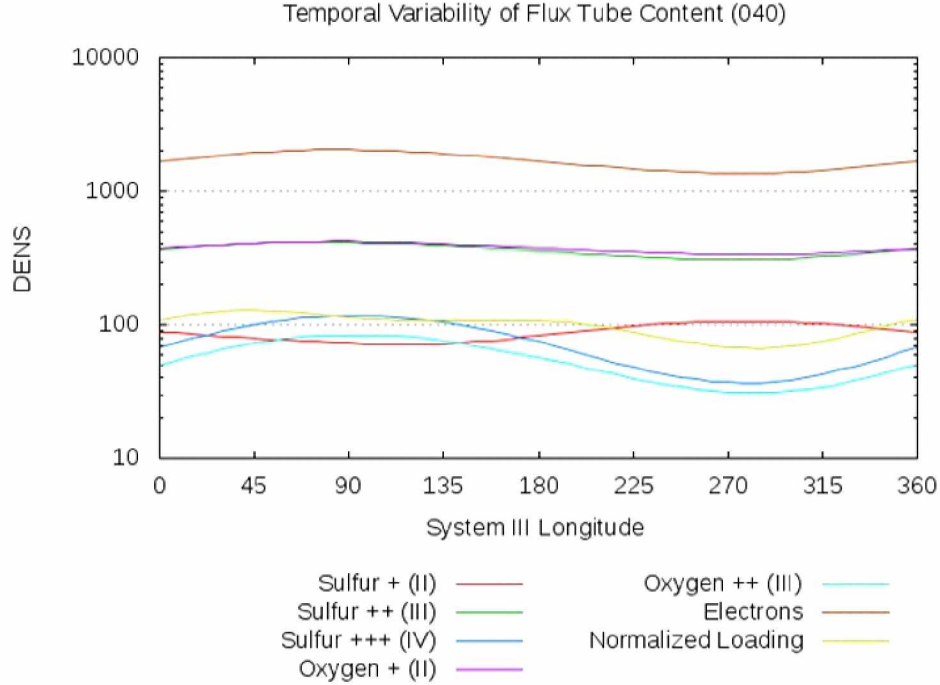
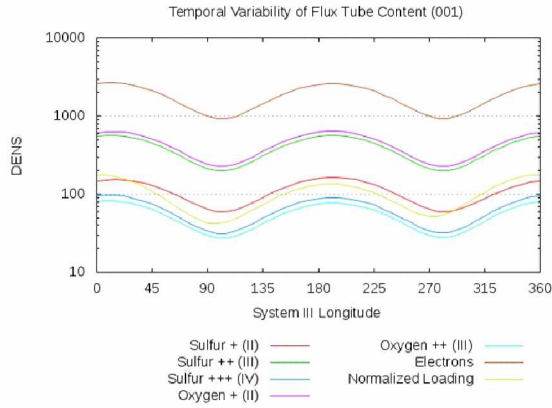


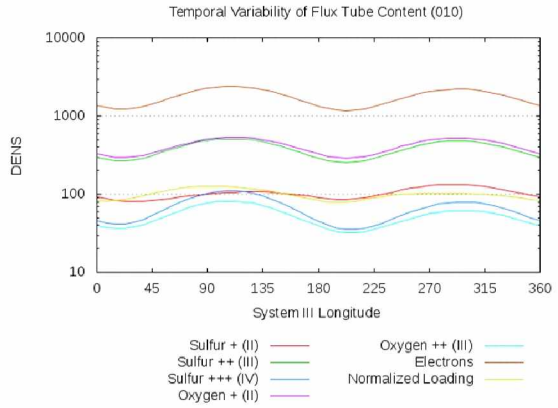
Figure 10: Dual hot electron model output showing azimuthal density variation in particles per cubic centimeter.

known that the plasma torus has a single-peaked azimuthal variation, but this occurs in spite of two peaks in neutral density where the plasma torus and neutral torus intersect. One might expect to see a peak at both points of intersection but observations clearly show a single peak. This implies that neutral density is not the most important factor in creating this peak. The peak must be attributed to increased generation of plasma locally.

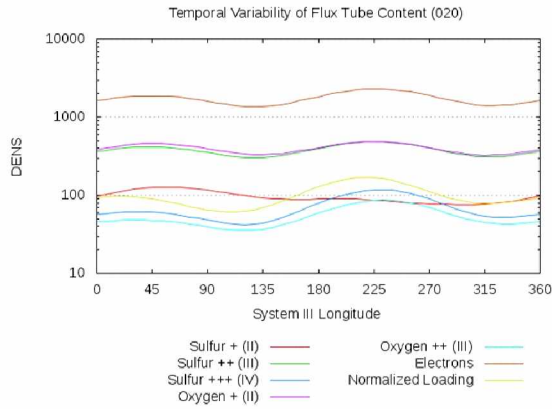
Our model already generates a single-peaked structure, which is to be expected with hot electron modulation, but what happens if the system is initialized with two peaks? Can a two peak structure be sustained, and how will the evolution of the structure occur?



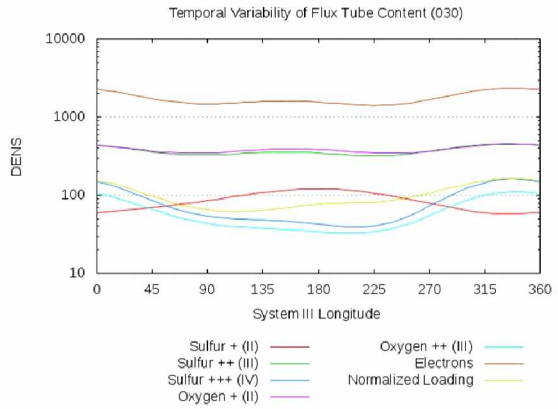
(a) The initialized two peak variation after one day



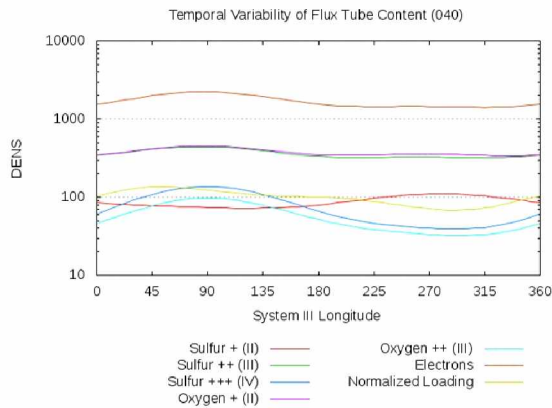
(b) Day 10



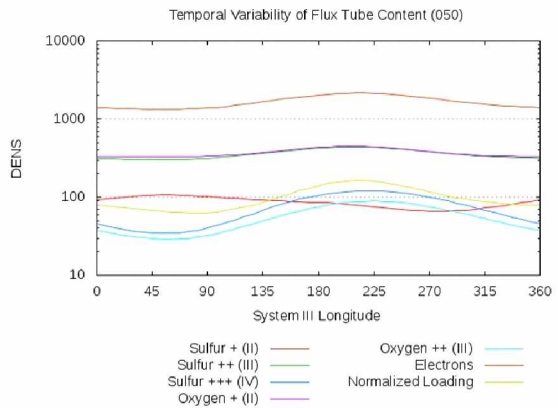
(c) Day 20



(d) Day 30



(e) Day 40



(f) Day 50

Figure 11: Evolution of two peaked wave structure in the torus. Densities in particles per cubic centimeter.

Table 3: Input parameters that produce phase shifts in System IV.

Parameters	Values
Neutral Source Rate	$1 \times 10^{28} \text{ s}^{-1}$
Hot Electron Fraction	0.15%
System III Hot Electron Variation	50%
System IV Hot Electron Variation	20%
Subcorotation Velocity	$1.5 \text{ km/s}$

We initialized our model with a uniform neutral source and a two peaked plasma density structure such that  $n = A \cos 2\theta$ , and showed that it does indeed become a single peak over time as shown in Figure 11. The mechanism responsible for azimuthal variation is not the off axis tori, but the hot electrons. The hot electron interactions occur at a much shorter timescale than plasma-neutral reactions and can thus generate large localized variations that could not otherwise be explained. The result suggests hot electrons play a large role in the dynamics of the torus.

## 2.5 Transient Wave Motion

We investigated the wandering System IV variation using a similar model to the *Steffl et al.* [2008] dual hot electron model. The variations in composition, temperature, and density are single-peaked and behave as a wave moving in System III. From here forward, wave will refer to these variations, such as density and mixing ratios, as opposed to MHD waves. System IV has been known to shift suddenly and was described by *Brown* [1995] as “sudden but reversible phase changes”. Motivated by these observations we looked at what parameters might produce similar results in our model.

To create phase changes in the model, we looked to the parameters that created the periodicity, see Table 3. By changing the abundance of hot electrons in System III and System IV we were able to observe growing and diminishing amplitude of the System IV variation of mixing ratios [*Steffl et al.*, 2008]. The variation was greatest when the System III and System IV hot electrons peaked at the same place. As System III and System IV populations moved out of phase the amplitude would diminish. If System IV was too weak,

the variation would remain stationary in System III, and when System IV was strong the variation would travel almost uniformly through System III. System IV hot electrons can be adjusted such that the wave will travel in System III but diminish when System IV is out of phase. With this critical System IV hot electron abundance, the model would produce a phase shift as the peak mixing ratio would diminish and almost immediately reform in the location enhanced System III hot electrons as shown in Figure 12. Once System IV and System III hot electron populations were in phase again, the density peak would begin propagating and diminishing as it had before.

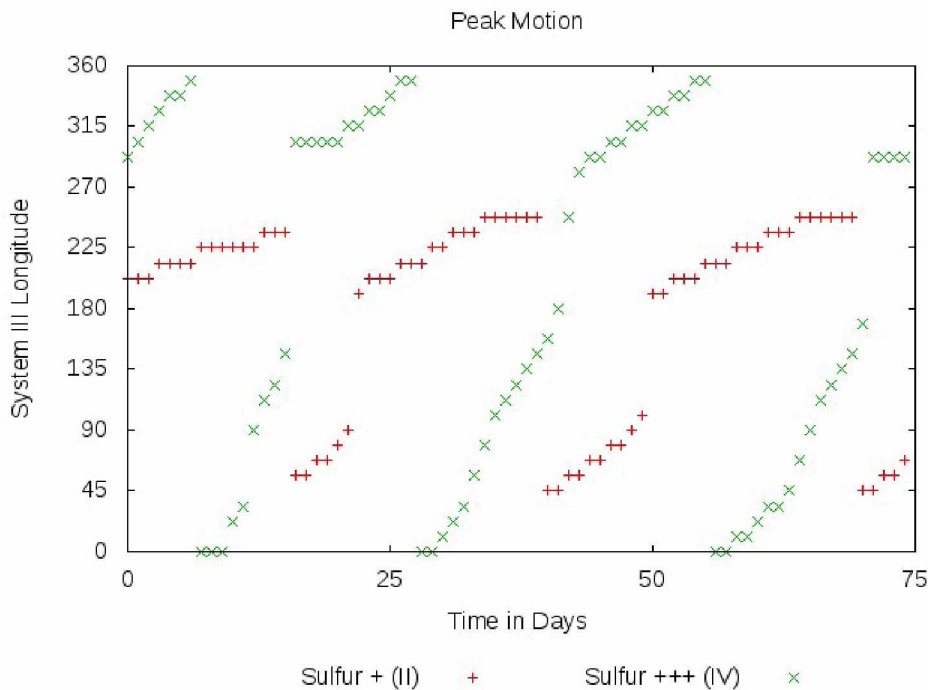


Figure 12: The motion of the peaks of  $S^+$  and  $S^{+++}$  mixing ratios in System III.

The reason the peak is able to immediately proceed after the phase change is that the formation of the peak occurs at the beat frequency of System III and System IV while the density peak moves with subcorotation, which is prescribed to be different from System IV period, in the absence of highly abundant System IV hot electrons. The perturbation in System III forms when there is constructive interference, then moves with System IV hot electrons.

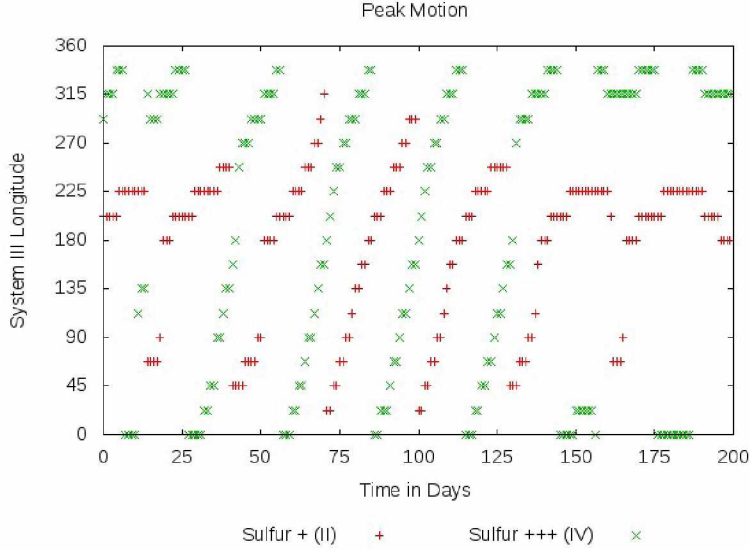


Figure 13: Peak motion in System III with a Gaussian perturbation of hot electron abundance.

With a critical input of System IV hot electrons, the density peak forms and moves in System III, but once it is in motion, the wave is more greatly affected by subcorotation than hot electrons. If there are enough System IV hot electrons, the plasma can be generated fast enough to sustain a subcorotating wave form. With System IV velocity varying from subcorotation, the generation of plasma is out of phase with the motion of the existing peak and the peak diminishes while moving at subcorotation velocity. Once there is constructive interference again, the peak forms again and begins to propagate. In the absence of System IV hot electrons, the peak forms but does not propagate and is instead offset from the peak of System III hot electrons.

The conditions necessary to produce these phase shifts may be the norm for the torus or may be onset during volcanic activity on Io that causes increased hot electron production. We have also modeled a scenario where hot electrons are added to the torus as a time varied Gaussian with a peak of thrice the hot electron abundance. What is seen is strong System IV trends during the eruption and transient wave motion during calm torus conditions, as in Figure 13. The changing hot electron abundance can affect System IV phase and can create situations where the wave motion is strongly coupled to System IV, poorly coupled,

or barely any coupling at all.

## 2.6 Mass Loading

It has been suggested that subcorotation of the plasma in the torus may be a result of mass loading of the magnetic field [*Pontius and Hill*, 1982]. If this is true, the subcorotation would vary in azimuth. With our model we simulate this hypothesis by modulating subcorotation as a function of mass loading. *Pontius and Hill* [1982] suggest that subcorotation velocities could be calculated as shown in Equation 8, where  $v_{co}$  is corotation velocity,  $\dot{M}$  is mass loading rate,  $\Sigma_P$  is Pederson conductivity,  $R_J$  and  $B_J$  are the radius and equatorial magnetic field of Jupiter, and  $L$  is the radial distance in Jovian radii.

$$\delta\omega = \frac{v_{co}\dot{M}L^4}{4\pi\Sigma_P R_J^3 B_J^2 \Delta L \sqrt{1-1/L}} \quad (7)$$

$$u = \frac{v_{co}\dot{M}L^5}{4\pi\Sigma_P R_J^2 B_J^2 \Delta L \sqrt{1-1/L}} \quad (8)$$

The concept is that each pick-up ion has its guiding center moved radially outward by one gyroradius, creating a current proportional to the amount of mass loading. The current generated by the pickup process must map to a current in the ionosphere, as shown in in Figure 14, that can be calculated using Ohm's law. The ionospheric current is dependent on subcorotation of the plasma. Equating these two currents, *Pontius and Hill* [1982] create an expression for subcorotation in terms of mass loading, Equation 7.

We adjusted parameters to see if we could create periodicities driven solely by variation in subcorotation. The idea is that as mass loading occurs in an area, subcorotation will increase, which results in plasma having greater subcorotation velocity in System III. This propagates the high density region of the torus created by mass loading and creates a feedback wherein regions of greater mass loading transport plasma to more rigidly corotating regions where there is less mass loading. The plasma then collects in the previously stagnant region and mass loading increases thus continuing the feedback. Results using this approach are show

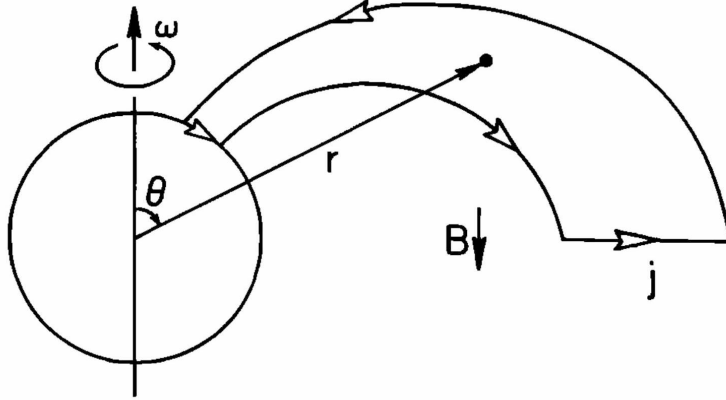


Figure 14: Diagram of the current loop that *Pontius and Hill* [1982] suggest is responsible for subcorotation in the torus.

in Figure 15. With variable azimuthal flow velocity, the upwind scheme had to be modified, as shown in Equation 9, into flux conservative form.

$$n_i^{j+1} = n_i^j + \frac{\Delta t}{\Delta x} [u_{i-1}^j n_{i-1}^j - u_i^j n_i^j] \quad (9)$$

In Equation 8 all variables are either well known or calculated within the model, with the exception of, the Pederson conductivity,  $\Sigma_P$ . We can vary mass loading to a small extent by varying the neutral source rate, but neutral source rates are only observed to vary from 500 kg to 2000 kg [*Delamere and Bagenal*, 2003]. The Pederson conductivity is suggested to be between 0.1 mhos and 10 mhos, but even at 0.1 mhos the subcorotation is less than 1 km/s. This means that the Pederson conductivity is lower than previously believed or that mass loading is not the only cause of subcorotation in the torus.

In addition to subcorotation, mass loading could have an affect on hot electron production. *Barbosa* [1985] suggests that ionization of neutrals could be a primary electron heating mechanism. Though this mechanism was suggested, there is no way to determine the exact result of mass loading on electron temperature. Motivated by *Barbosa* [1985] and *Pontius and Hill* [1982], we modulate hot electron fraction and subcorotation as a function of mass loading. We also assume that another mechanism must be facilitating subcorotation and



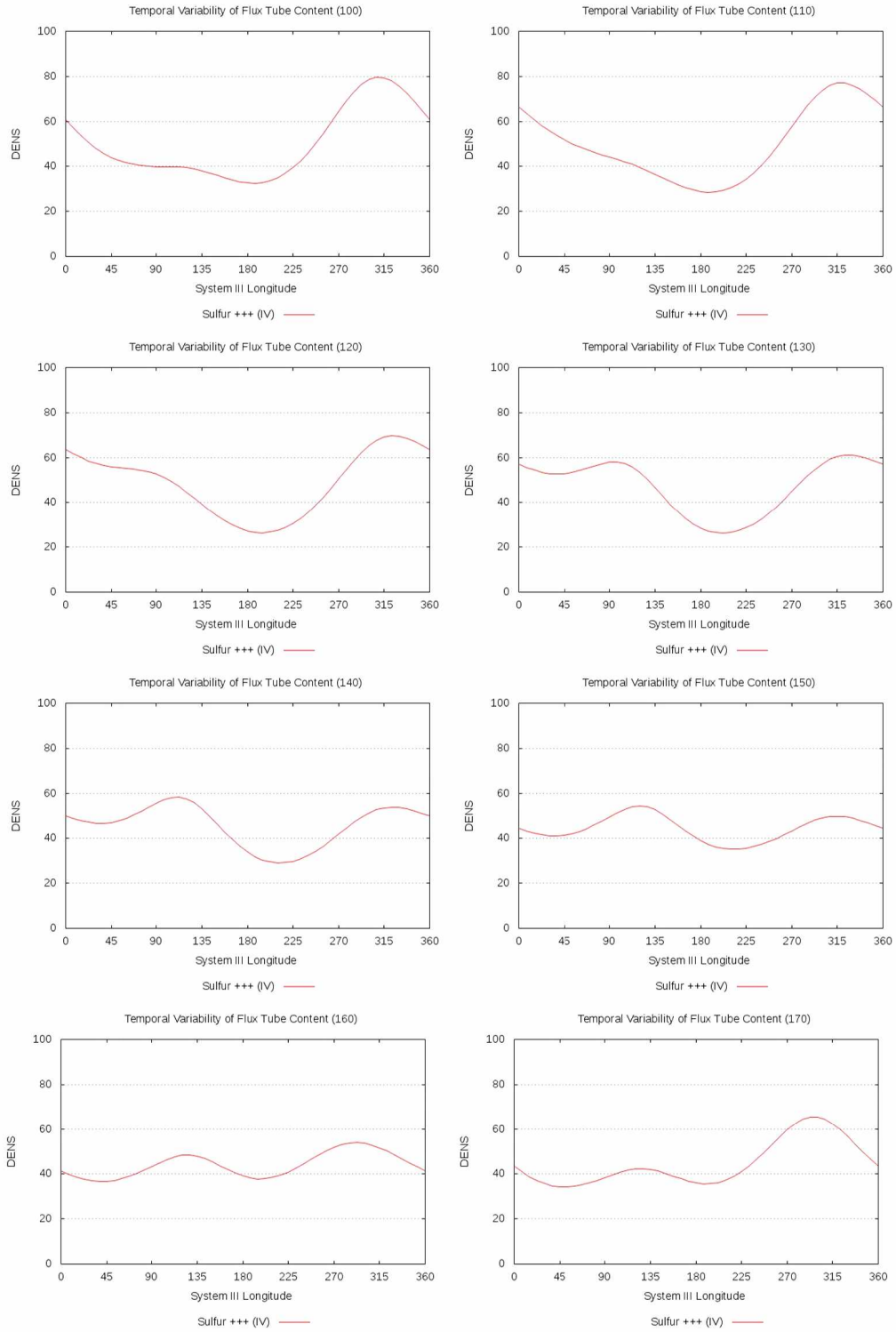


Figure 15: Azimuthal density variations generated by modulating subcorotation velocity with local mass loading. All hot electron variations are stationary in System III. Each frame is ten days apart.



add a constant 0.5 km/s to the subcorotation velocity calculated with the *Pontius and Hill* [1982] description. Figure 16 shows a large amplitude variation and faster propagation. The addition of hot electron modulation has made this a more viable approach, however it still fails to recreate some important torus observations, such as peaks in  $S^+$  and  $S^{+++}$  density that are  $180^\circ$  out of phase. Perhaps, with the right combination of subcorotation and hot electron modulation we could recreate observations in the future.

## 2.7 Summary

We have used the one-dimensional, azimuthal model to investigate the wave nature of the torus and the possible drivers of these variations. System III and IV hot electron abundance were adjusted to show how they might cause the phase shift of System IV density variations observed by [Brown, 1995]. It was also suggested that the coupling of System IV may be very strong or very weak depending on torus conditions. We also demonstrate that torus fluctuation are not primarily affected by overlap of neutral and ion populations which orbit on different axes. If this were the case one would expect two peaks corresponding to the intersections however, even when the torus is initialized with two peaks, it evolves into a single-peaked structure driven by hot electron variation. We then consider how momentum transfer and subcorotation may drive torus variation without the use of an ad hoc System IV hot electron population. It was shown that peaks, generated by hot electrons confined in System III, can be propagated by subcorotation variations dependent on mass loading as outlined in [Pontius and Hill, 1982]. With the addition of hot electrons created through mass loading, as suggested by Barbosa [1985], we can more closely recreate behavior like System IV, however this method still fails to display the  $180^\circ$  phase difference between  $S^+$  and  $S^{+++}$ .

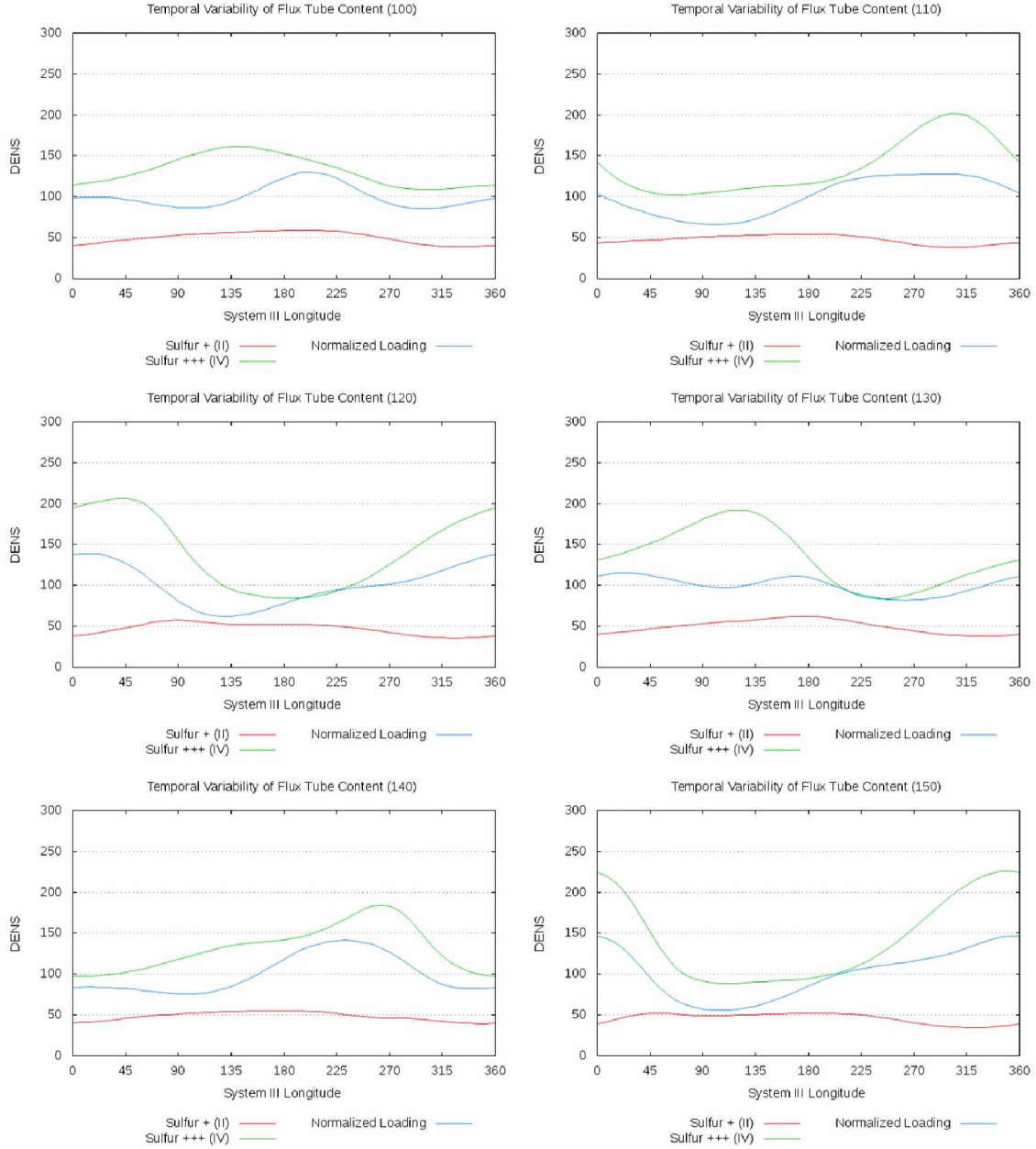


Figure 16: Azimuthal density variations generated by modulating subcorotation velocity and hot electrons with local mass loading. Each frame is ten days apart.

## Chapter 3 Radial Variation

We now move from one-dimensional azimuthal modeling to modeling that includes radial variation. The radial dimension adds the need for radial transport and radially dependent hot electron fraction and neutral source rate. Radial transport is handled using the diffusion equation for magnetospheric plasma [Roederer, 1970],

$$\frac{\partial Y}{\partial t} = L^2 \frac{\partial}{\partial L} \left( \frac{D_{LL}}{L^2} \frac{\partial Y}{\partial L} \right), \quad (10)$$

and communication between processors. It should also be noted that  $D_{LL}$ , the diffusion coefficient, is radially dependent and is assumed to have the form  $D_{LL} = D_{LL_0}(L/L_0)^\alpha$ , where  $\alpha > 0$ , and  $L$  denotes the radial distance in units of  $R_J$ . In the diffusion equation,  $Y$  is a conserved quantity to be transported. We used mass per unit of magnetic flux,  $Y = NL^2$ , and energy per unit of magnetic flux,  $Y = NL^2TL^{8/3}$ , as the conserved quantities.

To handle transport,  $Y$  must be calculated by integrating density along field lines, as shown in Equation 11.

$$NL^2 = 4\pi R_J^3 L^4 \int_{\theta=0}^{\theta_{max}} n \cos^7(\theta) d\theta \quad (11)$$

Then, after transport rates are calculated, the quantities must be converted back to density and energy with an iterative Newton-Raphson scheme. The diffusion equation approximates the dynamics of the torus, though actual transport is more complicated and involves flux tube interchange. The diffusion equation describes the general nature of diffusive transport however, we must transform it to fit our needs. This means that it must be made to be solved numerically rather than its previous analytic form.

### 3.1 Transport

To solve Equation 10 numerically, we use the numerical scheme given in Equation 12. We substitute  $NL^2$ , the flux tube mass content, for  $Y$  as an illustration. In Equation 12, the

subscript denotes the radial bin where  $i - 1$  is the bin radially inward and  $i + 1$  is radially outward. The processors are identified by an ID number that acts as a one-dimensional array while the model is two-dimensional. To translate from a two-dimensional array of bins to a processor ID we arrange our processors such that they are consecutive azimuthal arrays. For  $N$  azimuthal bins and  $M$  radial bins, the first  $N$  processors would be at the innermost radius and the next  $N$  processors would be  $\Delta L$  outward, and so on. In Equation 12, processor  $i - 1$  is actually the current processor minus  $N$  and, similarly,  $i + 1$  is the current ID plus  $N$ .

$$(NL^2)_i^{j+1} = \Delta t \left\{ (L^2)_i^j \frac{1}{(\Delta L)^2} \left[ \left( \frac{(D_{LL})_{i+1/2}^j}{(L^2)_{i+1/2}^j} ((NL^2)_{i+1}^j - (NL^2)_i^j) - \left( \frac{(D_{LL})_{i-1/2}^j}{(L^2)_{i-1/2}^j} ((NL^2)_i^j - (NL^2)_{i-1}^j) \right) \right] \right\} + (NL^2)_i^j \quad (12)$$

This method of locating processors by their ID also requires one alteration to the previously stated azimuthal transport method. We had said that processor  $N - 1$  is to the left of processor 0, and vice versa, this configuration holds true, however it is not a general expression for all azimuthal boundaries. To create a general expression we will introduce  $m$  as the order of the radial ring a processor resides in and  $n$  as the azimuthal arm where the processor conceptually resides, and both start from 0 like the processor IDs. The boundaries are at processor  $mN$  and  $(m + 1)N - 1$  and that they neighbor each other such  $mN$  is to the right. In general the processor to the left is  $mN + (n - 1)(\text{mod } N)$  and to the right is  $mN + (n + 1)(\text{mod } N)$ . Radially, we add  $N$  to get the ID of the outer processor and subtract  $N$  to find the ID of the inner processor as long as it is not at a boundary. Since the radial dimension is not circular, boundaries must be handled differently.

The transport must be handled empirically at the boundaries in order to simulate the physical reality. There is no general method of handling radial boundaries. For example, there is effectively no plasma being transported in at the inside boundary and so the boundary condition must reflect that. At the outside boundary we assume that  $NL^2$  has a set value

that has been predetermined based on UV observation [Bagenal, 1994].

Our model considers the transport of each species separately such that the gradient in  $NL^2$  for each species decides the transport of that species. For example,  $O^{++}$  may transport inward while  $O^+$  is transported outward. The diffusive transport equation does not perfectly describe transport in the torus and this method of handling each species separately appears to best reflect observation. In spite of this unphysical way to handle transport, our model can accurately fit the observations. The model will be inherently incapable of achieving a perfect fit because we are modeling a dynamic system with some static input parameters such as source rate and electron distribution (prescribed by the fraction of electrons that are hot electrons).

### 3.2 Agreement with Observations

Before continuing to experiment in two dimensions, we must verify that the model behaves correctly in the new radial dimension. Using observations derived from UVIS data by *Steffl et al.* [2008], we adjust model parameters, such as source rate, hot electron fraction,  $D_{LL}$ , and their power law exponents, to match observations. In this case we compare our results to observed mixing ratios. Using all mixing ratios and the electron density, we can determine the accuracy of the radial chemistry profiles. In Figure 18, the model results are plotted as a solid red line, and each observation data point as green x with error bars. We can not expect to perfectly match observation with static inputs since changing parameters in the inner torus will propagate outward over time. While the line does not perfectly pass through each error bar, we can say that it fits closely.

*Delamere et al.* [2005] showed that integrated transport time was slightly longer than expected when compared to *Schreier et al.* [1998]. In the current model, this is not the case and expected integrated transport time is within the range of possibility. In Figure 17, the integrated transport time to  $9 R_J$  is about 70 days. An integrated transport time of 11 – 60 days has been suggested by *Bagenal and Delamere* [2011]. A higher  $D_{LL}$  will result in faster

transport.

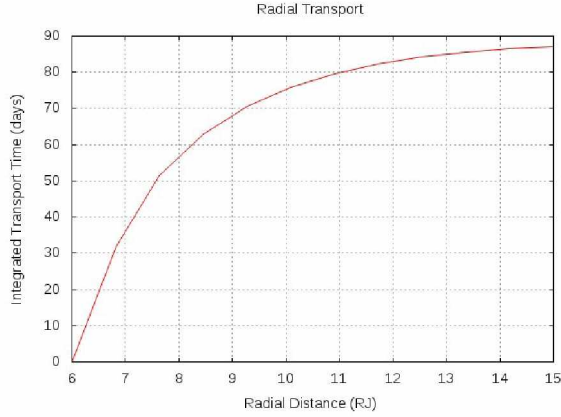


Figure 17: The integrated transport time of plasma moving radially in the torus.

### 3.3 Inferences and Analysis

Based on what we know about torus conditions we can use the model to infer other information. To show this, we have tested the goodness of fit for a range of source rates and transport rates through  $D_{LL}$ , the diffusion coefficient. After running the model for many combinations of source and transport rates, we can calculate a  $\chi^2$  or reduced  $\chi^2$  value, as shown in Equation 13, for each run and plot goodness of fit as a function of the inputs.

$$\chi^2 = \sum_i \frac{(O - E)^2}{\sigma^2} \quad (13)$$

To calculate reduced  $\chi^2$ , divide  $\chi^2$  by the degrees of freedom,  $\nu$ . This process can be replicated for any parameters. The results in Figure 19 show the parameters of best fit within the parameter space using a heat-map where blue represents the lowest  $\chi^2$  value and best fit. The observations of mixing ratios, electron temperatures, and column integrated density were all derived from Cassini UVIS data by *Steffl et al.* [2004]. Neutral source rate and diffusion coefficient were varied and all other parameters, including radial dependence, are similar to the parameters found in *Delamere et al.* [2005] using a different method. With enough observations, you can attempt infer any information that can be varied in the model.

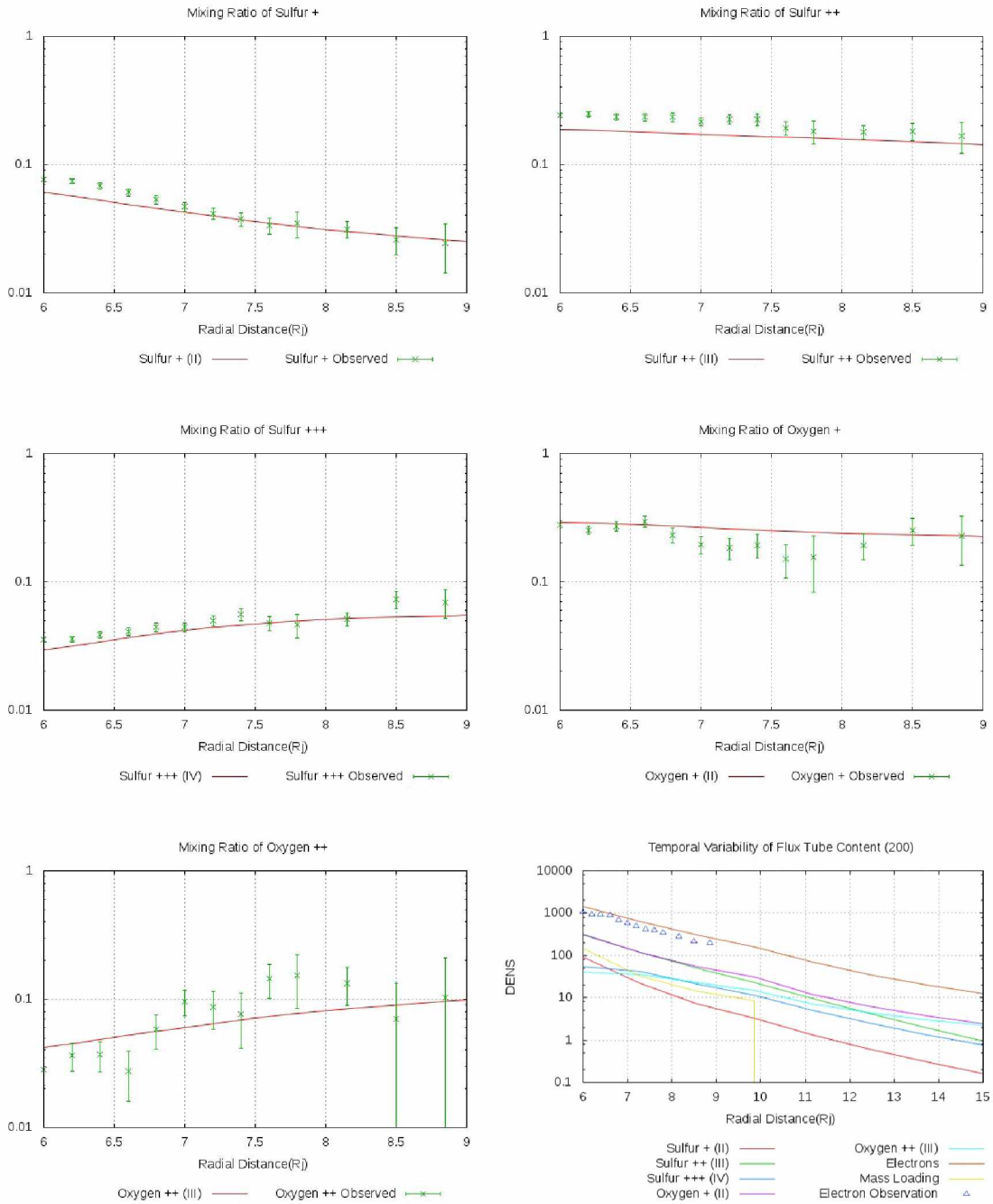


Figure 18: Agreement between output from the model with observation of radial variation. The first five plots are mixing ratios of each species and the last is the radial density profile with observed electron densities.

We find a best fit with a neutral source rate of  $\sim 5 \times 10^{27}$  particles per second (or about 167 kg/s) and a  $D_{LL}$  of  $\sim 3 \times 10^{-7} s^{-1}$ .

With more observational data, we can better infer other parameters. We can overlay contours of other outputs like power radiated and show another constraint for the fit. Similarly, we could do this with ion temperatures, integrated transport time, and any other constraint. The best constraint would be one that has best fits along a line perpendicular to the current best fit contours. This would narrow down the parameters to the location where both contours intersect and would much more tightly constrain our parameters. The goodness of fit plots are can be a great tool for better estimating unknowns about the torus and advancing our understanding.

This analysis also emphasizes the need for an efficient parallel program. To analyze goodness of fit in a parameter space we must run the model for a range of inputs for the two parameters used. In addition to source rate and diffusion coefficient, the model is able to do a similar analysis with Oxygen to Sulfur ratio of the neutral source, hot electron fraction, hot electron temperature, and the radial dependence (by way of exponent in power law) of source rate, diffusion coefficient, and hot electron fraction. We can also easily adapt the model for other parameters as necessary. To get a grid resolution of ten by ten, the model must be run one hundred times. Any lower resolution and the parameters that produce the minimal  $\chi^2$  can not be determined with the same accuracy.

This model has clear potential as a tool for researchers to better understand and utilize observations. With more observations, like those of the current Hisaki, or Sprint-A, mission, we will be able to much better infer the more difficult to measure parameters.



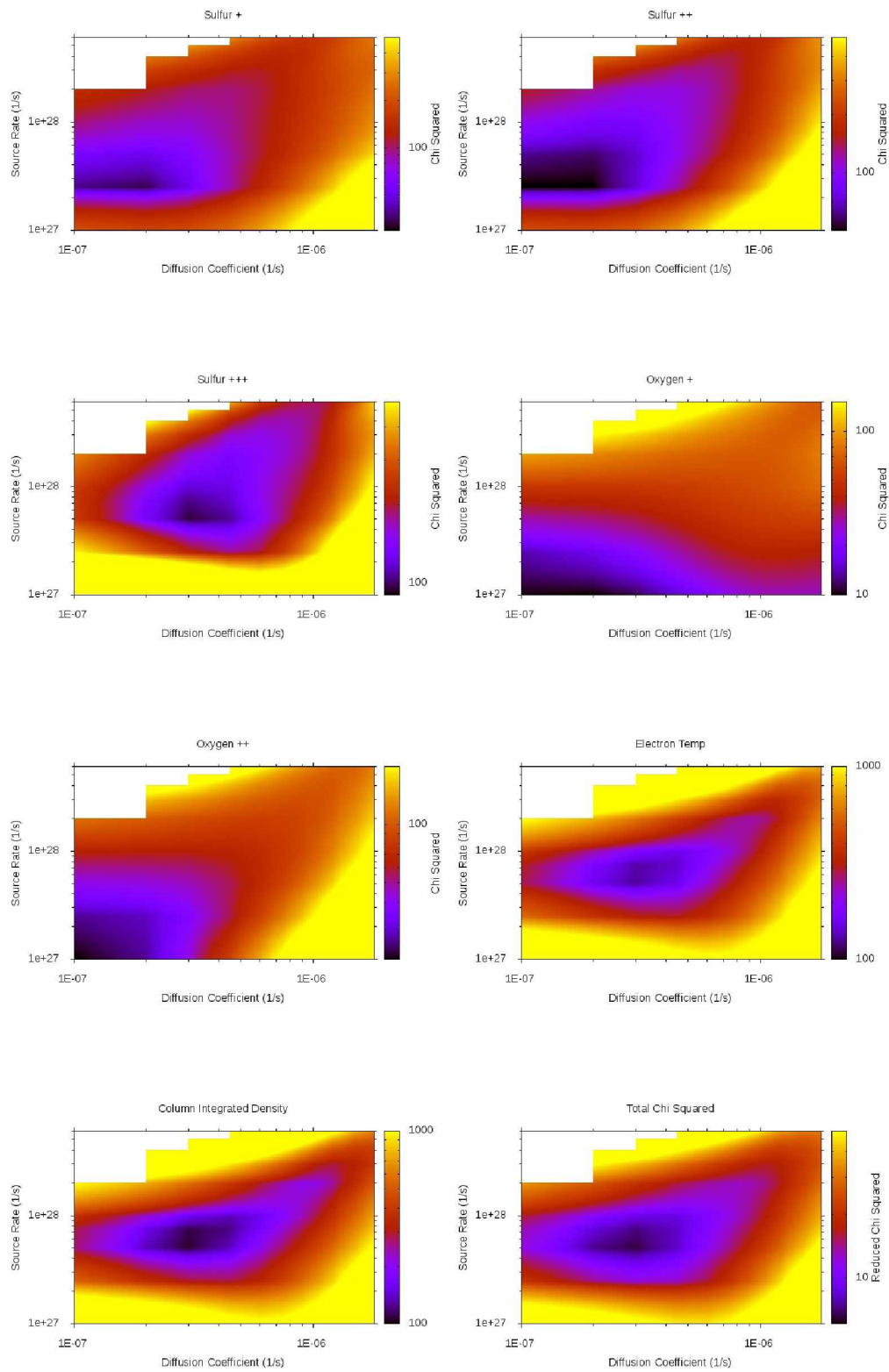


Figure 19: Chi squared plots for varied neutral source rate and diffusion coefficient. Thirteen observations were used to calculate chi for each of the seven parameters.

## Chapter 4 Two Dimensional Model

With azimuthal and radial dimensions verified and working as expected, the two can be looked at simultaneously. While both dimensions can be modeled separately, it is probable that the dynamics of each dimensions may be affected by the other. An example of this would be the peak in densities in System III being damped by locally increased diffusive radial transport due to increased radial gradients. For this reason, we should revisit some previous results with this two-dimensional model and verify that the observable torus dynamics are still present in the model.

Starting with the basic model, we verify that System III and System IV hot electrons can create a subcorotating density peak, as was previously observed in the azimuthal model. In addition to verifying the model, we can see if such a system can create coherent radial structure outside of the inner torus. Observations indicate that we should indeed see radially persistent structure in  $S^+$  [*Brown, 1995*], but it is unclear what mechanisms support this structure while the plasma is subjected to an azimuthal shear.

In Figure 20 we show model results using System III and IV hot electrons to create a single-peaked structure. The model does not yet contain azimuthal shear, but does have diffusive radial transport and uniform subcorotation. The azimuthal modulation of hot electron populations (background multiplied two sinusoids with different amplitudes) are uniform in radius. With an integrated transport time that is longer than the System IV period and subcorotation period, there would be a dramatic swirling effect if variations outside the inner torus were a result of transport alone. The plots show that the radial structure seems to be driven by hot electron variation rather than diffusive transport. Future work will account for radial shears.

Because the radial transport may act to damp azimuthal variations in the torus, we should also recreate the previous results that modulate subcorotation with mass loading as suggested by *Pontius and Hill* [1982]. This mechanism was capable of producing a feedback

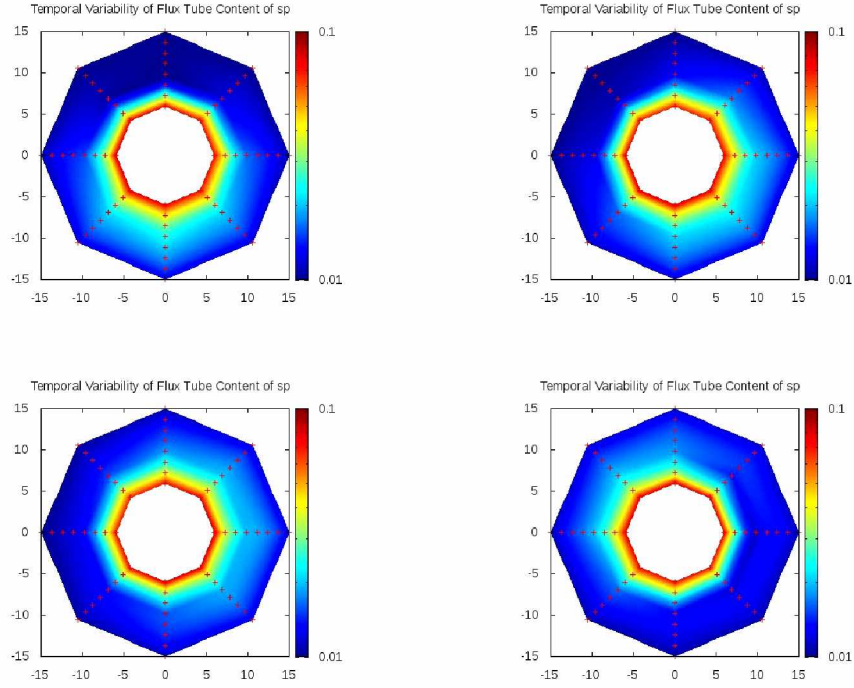


Figure 20: System IV variations of  $S^+$  in two dimensions. In the presence of diffusive radial transport, hot electrons can still produce a single-peaked structure. The time progression of these plots goes left to right. Colors denote local mixing ratio.

that would create and propagate an azimuthal structure. With radial transport, the damping may cause the mass loading to be insufficient to create a feedback loop. When modeled, the torus has a single peak that does not move in System III and is anchored by the hot electrons that are stationary in System III.

While the radial transport may damp azimuthal variation, *Hess et al.* [2011] suggests that radial transport may lead to more hot electrons through flux tube interchange events. Such a mechanism could continue to drive azimuthal variation beyond the inner torus. We will likely revisit this topic and experiment with the model by increasing the hot electron fraction as a function of radial transport.

## Chapter 5 Conclusions

The work done over the last two years has produced a model that has already shown its potential as a necessary and useful tool for testing hypotheses, inferring important information, and understanding observations of the Io plasma torus. We have modeled neutral input, chemical reactions, azimuthal and radial transport to capture the behavior of the torus as observed by Voyager and Cassini spacecraft. Our work has been verified and validated by previous work and observations, and our experimentation has yielded important insight.

We have shown the necessity of azimuthally modulated hot electrons in the torus to produce the observed single peak density structure through rapid chemical reactions. Our modeling of mass loading as suggested by *Pontius and Hill* [1982] has shown the plausibility of mass loading of the torus contributing to subcorotation in the inner plasma torus, though much closer to corotation than observed. In addition, we have shown that a critical combination of System III and System IV hot electrons is a likely cause for the transient System IV behavior observed by *Brown* [1995].

Due to the efficiency and scalability of the parallel two-dimensional model we can create useful plots that determine goodness of fit relative to observed data and infer the most likely conditions that would lead to observed conditions. This will allow us to better understand how torus parameters can affect observations. With observations from the EXCEED instrument on-board the Hisaki satellite, this model can be used to quickly make inferences and utilize any new information about the torus. Below is a summary of our findings.

- We investigated the single-peaked nature of the torus and concluded that hot electrons played a larger role in local torus dynamics than neutral and plasma torus offset due to the shorter timescale of hot electron reactions that create  $S^+$  and  $S^{+++}$ .
- By adjusting the modulation of hot electrons in System III and IV, we were able to replicate the observations by *Brown* [1995] and suggest that variations of the hot electron populations can cause System IV to phase shift.

- Following the work of *Pontius and Hill* [1982], we calculated subcorotation velocities as a function of mass loading to show that it does create variable subcorotation that can produce a moving structure, but that it was insufficient to fully explain the larger observed subcorotation velocities, for the range of published values for  $\Sigma_P$  and  $\dot{M}$ .
- We introduced Chi Squared analysis to the topic of the Io plasma and showed its usefulness in inferring torus parameters. We determine the best fit occurred when neutral source rate was  $\sim 5 \times 10^{27}$  particles per second (or about 167 kg/s) and  $D_{LL}$  was  $\sim 3 \times 10^{-7} s^{-1}$ .
- We have showed the importance of two-dimensional modeling and the potential coupling that can occur, especially when relying on a feedback mechanism. Radial transport does damp azimuthal variation.

In the future, research will continue by using this model to do a more complete analysis of goodness of fit by further confining results using constraints on power radiated, integrated transport time, and ion temperatures. We will also examine other parameter sets in order to investigate how all the parameters affect torus composition and observations. The two-dimensional model will be used to look at what causes persistent radial structure while the torus is subjected to azimuthal shear flows. This will be done by looking at the curvature of the radial peak or ridge in densities of given species. If the structure is created only by transport of material from the interior, the radial ridge will have a curve such that the peak at  $9 R_J$  is offset from the peak at  $6 R_J$  by the integrated transport time. Alternatively, a perfectly radial curve would indicate that the structure is fueled by azimuthal variation of hot electron abundance.

This research has yielded important results pertaining to the nature of torus dynamics. We hope that this tool can be used to analyze future observations and investigate theories that were previously unable to be modeled. I submit that beyond the advancement of the topics herein, this work can continue to further our understanding of the torus by enabling

researchers to easily test and adapt theories.

## References

- Bagenal, F. (1994), Empirical model of the Io plasma torus: Voyager measurements, *99*, 11,043–11,062, doi:10.1029/93JA02908.
- Bagenal, F., and P. A. Delamere (2011), Flow of mass and energy in the magnetospheres of Jupiter and Saturn, *Journal of Geophysical Research (Space Physics)*, *116*, A05209, doi:10.1029/2010JA016294.
- Bagenal, F., T. E. Dowling, and W. B. McKinnon (2004), *Jupiter : the planet, satellites and magnetosphere*.
- Barbosa, D. D. (1985), Thermalization of neutral-beam-injected ions by lower hybrid waves in Jupiter's magnetosphere, *Physical Review Letters*, *54*, 1160–1162, doi:10.1103/PhysRevLett.54.1160.
- Barbosa, D. D., F. V. Coroniti, and A. Eviatar (1983), Coulomb thermal properties and stability of the Io plasma torus, *Astrophysical Journal*, *274*, 429–442, doi:10.1086/161459.
- Brown, M. E. (1994), Observation of mass loading in the Io plasma torus, *Geophysical Research Letters*, *21*, 847–850, doi:10.1029/94GL00564.
- Brown, M. E. (1995), Periodicities in the Io plasma torus, *Journal of Geophysical Research*, *100*, 21,683–21,696, doi:10.1029/95JA01988.
- Burger, M. H. (2003), Io's neutral clouds: From the atmosphere to the plasma torus, Ph.D. thesis, UNIVERSITY OF COLORADO AT BOULDER.
- Connerney, J. E. P. (2007), Planetary magnetism, *Treatise in Geophysics*, *10*.
- Connerney, J. E. P., M. H. Acuña, N. F. Ness, and T. Satoh (1998), New models of Jupiter's magnetic field constrained by the Io flux tube footprint, *Journal of Geophysical Research*, *103*, 11,929–11,940, doi:10.1029/97JA03726.

- Delamere, P. A., and F. Bagenal (2003), Modeling variability of plasma conditions in the Io torus, *Journal of Geophysical Research (Space Physics)*, *108*, 1276, doi:10.1029/2002JA009706.
- Delamere, P. A., F. Bagenal, and A. Steffl (2005), Radial variations in the Io plasma torus during the Cassini era, *Journal of Geophysical Research (Space Physics)*, *110*, A12223, doi:10.1029/2005JA011251.
- Dessler, A. J. (1983), *Physics of the Jovian magnetosphere*.
- Hess, S. L. G., P. A. Delamere, F. Bagenal, N. Schneider, and A. J. Steffl (2011), Longitudinal modulation of hot electrons in the Io plasma torus, *Journal of Geophysical Research (Space Physics)*, *116*, A11215, doi:10.1029/2011JA016918.
- Huba, J. D. (2013), *NRL PLASMA FORMULARY Supported by The Office of Naval Research*, 1–71 pp., Naval Research Laboratory, Washington, DC.
- Landi, E., P. R. Young, K. P. Dere, G. Del Zanna, and H. E. Mason (2013), CHIANTI-An Atomic Database for Emission Lines. XIII. Soft X-Ray Improvements and Other Changes, *The Astrophysical Journal*, *763*, 86, doi:10.1088/0004-637X/763/2/86.
- Pontius, D. H., Jr., and T. W. Hill (1982), Departure from corotation of the Io plasma torus - Local plasma production, *Geophysical Research Letters*, *9*, 1321–1324, doi:10.1029/GL009i012p01321.
- Roederer, J. G. (1970), *Dynamics of geomagnetically trapped radiation*.
- Sandel, B. R., and A. J. Dessler (1988), Dual periodicity of the Jovian magnetosphere, *Journal of Geophysical Research*, *93*, 5487–5504, doi:10.1029/JA093iA06p05487.
- Schneider, N. M., and F. Bagenal (2007), *Io's neutral clouds, plasma torus, and magnetospheric interaction*, p. 265, Springer Praxis Books / Geophysical Sciences.



- Schneider, N. M., and J. T. Trauger (1995), The Structure of the Io Torus, *Astrophysical Journal*, *450*, 450, doi:10.1086/176155.
- Schreier, R., A. Eviatar, and V. M. Vasyliūnas (1998), A two-dimensional model of plasma transport and chemistry in the Jovian magnetosphere, *Journal of Geophysical Research*, *103*, 19,901–19,914, doi:10.1029/98JE00697.
- Shemansky, D. E. (1988), Energy branching in the Io plasma torus - The failure of neutral cloud theory, *Journal of Geophysical Research*, *93*, 1773–1784, doi:10.1029/JA093iA03p01773.
- Steffl, A. J., A. I. F. Stewart, and F. Bagenal (2004), Cassini UVIS observations of the Io plasma torus. I. Initial results, *172*, 78–90, doi:10.1016/j.icarus.2003.12.027.
- Steffl, A. J., P. A. Delamere, and F. Bagenal (2008), Cassini UVIS observations of the Io plasma torus. IV. Modeling temporal and azimuthal variability, *Icarus*, *194*, 153–165, doi:10.1016/j.icarus.2007.09.019.
- Yoshioka, K., G. Murakami, A. Yamazaki, F. Tsuchiya, T. Kimura, M. Kagitani, T. Sakanoi, K. Y. Uemizu, K. and, and M. Fujimoto (2014), Evidence for global electron transportation into the jovian inner magnetosphere, *Science*, p. 1581.

## Appendices

### Appendix A - One Box Model

Following *Barbosa et al.* [1983] and *Delamere and Bagenal* [2003], the equations responsible for handling torus dynamics of the one box model for each species,  $\alpha$ , are

$$\frac{\partial n_\alpha}{\partial t} = \mathcal{S}_m - \mathcal{L}_m, \quad (14)$$

and

$$\frac{\partial(\frac{3}{2}n_\alpha T_\alpha)}{\partial t} = \mathcal{S}_\mathcal{E} - \mathcal{L}_\mathcal{E}. \quad (15)$$

These are written for general sources and losses. The source of density for each species,  $n_\alpha$ , is

$$\mathcal{S}_m = I_{\alpha_-} n_{\alpha_-} n_e + I_{\alpha_-}^h n_{\alpha_-} n_{e,hot} + R_{\alpha_+} n_{\alpha_+} n_e + \sum_{\gamma,\beta} k_{\gamma,\beta} n_\gamma n_\beta, \quad (16)$$

where  $\alpha_-$  and  $\alpha_+$  denote lower ionization state and higher ionization state respectively. Electron impact ionization is denoted by  $I$  and  $I^h$  for hot electron impact ionization. Recombination of higher ionization states, shown as  $R$ , act as a source for lower ionization states. All other reactions are shown in the last term with reaction rates rates as shown in *Delamere and Bagenal* [2003]. Similarly, loss rates are,

$$\mathcal{L}_m = I_\alpha n_\alpha n_e + I_\alpha^h n_\alpha n_{e,hot} + R_\alpha n_\alpha n_e + \sum_\beta k_{\alpha,\beta} n_\alpha n_\beta + \frac{n_\alpha}{\tau}, \quad (17)$$

where  $\frac{n_\alpha}{\tau}$  is the radial transport loss term. Energy sources and losses are handled similarly.

The overall source of energy for a species,  $\alpha$ , is

$$\begin{aligned} \mathcal{S}_\mathcal{E} = & I_{\alpha_-} n_e n_{\alpha_-} T_{\alpha_-} + I_{\alpha_-}^h n_{e,hot} n_{\alpha_-} T_{\alpha_-} + R_{\alpha_+} n_{\alpha_+} n_e T_{\alpha_+} \\ & + \sum_{\gamma,\beta} k_{\gamma,\beta} n_\gamma n_\beta T_\beta + \sum_{\beta=i,e} \nu^{\alpha/\beta} n_\alpha (T_\beta - T_\alpha), \end{aligned} \quad (18)$$

where the last term describes the coulomb coupling with another species,  $\beta$ . The thermal equilibration rate of two Maxwellian distributed species interacting through Coulomb collisions is

$$\nu_e^{\alpha/\beta} = 1.8 \times 10^{-19} \frac{(m_\alpha m_\beta)^{1/2} Z_\alpha^2 Z_\beta^2 n_\beta \lambda_{\alpha\beta}}{(m_\alpha T_\beta + m_\beta T_\alpha)^{3/2}} \text{sec}^{-1}, \quad (19)$$

where  $\lambda_{\alpha\beta}$  is the coulomb logarithm [Huba, 2013], and the charge number is  $Z$ . The last term will act as a loss for some species but is included in the source calculation, because differentiating between cases is unnecessary. Thermal energy of pickup ions is assumed to be the kinetic energy gained from accelerating the particle to a nearly corotational state. The energy loss for a given species is

$$\mathcal{L}_E = I_\alpha n_e n_\alpha T_\alpha + I_\alpha^h n_{e,hot} n_\alpha T_\alpha + R_\alpha n_\alpha n_e T_\alpha + \sum_{\alpha,\beta} k_{\alpha,\beta} n_\alpha n_\beta T_\alpha + \frac{n_\alpha T_\alpha}{\tau}. \quad (20)$$

The average electron temperature is dependent on Coulomb coupling, radiative cooling, and transport loss. The equation for change in electron temperature is

$$\frac{\partial(n_e T_e)}{\partial t} = \sum_{\beta} \nu^{\beta/e} n_e (T_\beta - T_e) - \frac{2}{3} \sum_{\beta,\lambda} \rho_{\beta,\lambda} n_e n_\beta - \frac{n_e T_e}{\tau}, \quad (21)$$

where the first term is the result of Coulomb collisions, the second is the affect of radiative cooling, and the last is transport of electrons. The radiative rate coefficient is  $\rho_{\beta,\lambda}$ .

## Appendix B - Latitudinal Averaging

In order to account for the separation of plasma from the neutral clouds, we implement a latitudinal averaging method. The plasma torus and neutral clouds are on two different planes. The separation is longitudinally dependent and the populations intersect at two points on the torus. This method will essentially average the effective reaction rates in latitude. To do this we must describe the density of neutrals and plasma species in latitude. We use a Gaussian approximation such that the number of ions of a given species on a flux

tube is

$$N \equiv \int_{-\infty}^{+\infty} n(z)dz = n(0) \int_{-\infty}^{+\infty} e^{-z^2/H^2} dz = \sqrt{\pi}n(0)H , \quad (22)$$

where  $H \equiv \sqrt{2T_i(1 + Z_iT_e/T_i)/3m_i\Omega^2}$  is the plasma scale height,  $\Omega$  is the angular frequency of Jupiter's rotation ( $1.76 \times 10^{-4}$  rad/s) and  $n(0)$  is the density plane of the plasma torus, and the ion charge number is  $Z_i$ . Using the total number of ions of a species on a flux tube,  $N$ , the density in the torus plane is

$$n(0) = \frac{N}{\sqrt{\pi}H} . \quad (23)$$

With the density in the plane of the plasma torus,  $n(0)$ , we can now calculate the total flux tube integrated source rate for a species,  $\gamma$ , due to a reaction between ion species  $\alpha$  and  $\beta$ . We express this as

$$\frac{\delta N_\gamma}{\delta t} = \int_{-\infty}^{+\infty} kn_\alpha(z)n_\beta(z)dz = kn_\alpha(0)n_\beta(0)\sqrt{\pi}H' , \quad (24)$$

where  $k$  is the reaction rate coefficient and  $H' = \sqrt{(H_\alpha^2 H_\beta^2)/(H_\alpha^2 + H_\beta^2)}$ . Using Equations 23 and 24, we can calculate an updated density in the torus plane after a time,  $\delta t$ .

$$n_\gamma(0) = \frac{N_\gamma + \delta N_\gamma}{\sqrt{\pi}H_\gamma} \quad (25)$$

This is now used to handle the chemistry of ions reacting with other ions. For ions and neutrals reacting, we must account for the separation of the torus plane and the neutral orbital plane. We also have to account for the variation of the separation of the neutrals and plasma in System III. We write the integrated reaction rate of ions with neutrals, with an offset of  $z_o$  in the neutrals, as

$$\frac{\delta N_\gamma}{\delta t} = kn_i(0)n_n(0) \int_{-\infty}^{+\infty} e^{-z^2/H_i^2} e^{-(z-z_o)^2/H_n^2} dz = kn_i(0)n_n(0) \sqrt{\frac{\pi}{a}} e^{(b^2-4ac)/4a} , \quad (26)$$

where  $a = (H_i^2 + H_n^2)/(H_i^2 H_n^2)$ ,  $b = -2z_o/H_n^2$ , and  $c = z_o^2/H_n^2$  to simplify the expression. Using quasi-neutrality, we can also say that

$$\frac{\delta N_\gamma}{\delta t} = kn_\beta(0) \sum_\alpha Z_\alpha n_\alpha(0) \sqrt{\pi} H' = kn_\beta(0) n_e(0) \sqrt{\pi} H_e , \quad (27)$$

where  $H' = (H_\beta^2 + H_\alpha^2)/(H_\beta^2 H_\alpha^2)$ , and  $Z_\alpha$  is the charge number. Hot electrons are modeled such that the fraction of electrons that are hot electrons,  $f_{eh}$ , remains constant. As such, the hot electrons are expressed as

$$\frac{\delta N_\gamma}{\delta t} = kn_\alpha(0) f_{eh} n_e(0) \sqrt{\pi} H_\alpha . \quad (28)$$

We can now model the affect of the separated neutral and plasma populations in the model and later adapt these methods to include azimuthal variation by calculating the offset,  $z_o$ , as a function of System III longitude.